

CellViT++: Energy-Efficient and Adaptive Cell Segmentation and Classification Using Foundation Models

Fabian Hörst^{a,b,c,1}, Moritz Rempe^{a,b,c}, Helmut Becker^{a,b}, Lukas Heine^{a,b}, Julius Keyl^{a,d}, and Jens Kleesiek^{a,b,c,e}

^aInstitute for AI in Medicine (IKIM), University Hospital Essen (AöR), Essen, Germany; ^bCancer Research Center Cologne Essen (CCCE), West German Cancer Center Essen, University Hospital Essen (AöR), Essen, Germany; ^cDepartment of Physics, TU Dortmund University, Dortmund, Germany; ^dInstitute of Pathology, University Hospital Essen (AöR), Essen, Germany; ^eGerman Cancer Consortium (DKTK, Partner site Essen), Heidelberg, Germany

Digital Pathology is a cornerstone in the diagnosis and treatment of diseases. A key task in this field is the identification and segmentation of cells in hematoxylin and eosin-stained images. Existing methods for cell segmentation often require extensive annotated datasets for training and are limited to a predefined cell classification scheme. To overcome these limitations, we propose CellViT++, a framework for generalized cell segmentation in digital pathology. CellViT++ utilizes Vision Transformers with foundation models as encoders to compute deep cell features and segmentation masks simultaneously. To adapt to unseen cell types, we rely on a computationally efficient approach. It requires minimal data for training and leads to a drastically reduced carbon footprint. We demonstrate excellent performance on seven different datasets, covering a broad spectrum of cell types, organs, and clinical settings. The framework achieves remarkable zero-shot segmentation and data-efficient cell-type classification. Furthermore, we show that CellViT++ can leverage immunofluorescence stainings to generate training datasets without the need for pathologist annotations. The automated dataset generation approach surpasses the performance of networks trained on manually labeled data, demonstrating its effectiveness in creating high-quality training datasets without expert annotations. To advance digital pathology, CellViT++ is available as an open-source framework featuring a user-friendly, web-based interface for visualization and annotation. The code is available under <https://github.com/TIO-IKIM/CellViT-plus-plus>.

Cells | Foundation Models | Digital Pathology | Segmentation | CV

Histopathology serves as the "workhorse" of medical diagnostics, playing a crucial role in the identification and classification of diseases. Through the systematic examination of tissue and cellular structures, pathologists generate important insights that inform clinical decision-making and influence treatment plans for various conditions, including cancer, infections, autoimmune disorders, genetic disorders, neurodegenerative diseases, cardiovascular diseases, or transplant rejection. For routine diagnostics, tissue samples are collected and stained with hematoxylin and eosin (H&E) to visualize cellular and tissue structures. The digitization of these tissue specimens through whole slide imaging (WSI) has introduced a significant advancement in pathology by enabling computational assessments (Song et al., 2023). This development facilitates the integration of artificial intelligence (AI) into diagnostic processes, enhancing existing workflows and slide quantification while advancing research and biomarker discovery. Consequently, more and more laboratories are shifting from traditional manual workflows to more efficient and scalable digitized workflows (Fraggetta et al., 2021; Baidoshvili et al., 2018). This process will be further expedited by the implementation of reimbursement strategies for medical AI solutions (Shafi & Parwani, 2023; Wu et al., 2023).

Among the various computational tasks in digital pathology, cell detection and classification in WSIs are particularly critical, as they can reveal prognostic factors. For example, tumor-infiltrating lymphocytes and inflammatory cells within the tumor microenvironment are important markers for breast cancer (Sun et al., 2021; Amgad et al., 2020). This task is not feasible for pathologists at a large scale due to its time-consuming nature and the high degree of intra- and inter-observer variability (Hörst et al., 2024a). Next to cellular detection, the precise identification of cell boundaries is essential for cellular feature analysis. Due to inconsistencies in cell morphology, staining intensity, and the presence of overlapping or touching nuclei, this task remains challenging. Deep learning methods based on convolutional neural networks (CNNs) (Naylor et al., 2019; Graham et al., 2019b; Stringer et al., 2021; Weigert & Schmidt, 2022) and Vision Transformers (ViTs) (Hörst et al., 2024a) have emerged as powerful tools in this context. In addition to algorithmic advancements, the digitization of pathology has led to the creation of increasingly large-scale slide datasets, predominantly by non-public institutions. This has facilitated the development of "foundation models" that are designed to learn generalizable representations from extensive amounts of WSI. Unlike specialized task-specific models, foundation models aim to serve as generalist models capable of addressing a wide range of tasks based on learned representations. Several foundation models have been proposed for digital pathology, including HIPT/HIPT₂₅₆ (Chen et al., 2022), UNI (Chen et al., 2024), Virchow (Vorontsov et al., 2024), Virchow₂ (Zimmermann et al., 2024), RudolfV (Dippel et al., 2024), and Gigapath (Xu et al., 2024), with the most promising models utilizing the ViT (Dosovitskiy, 2020) network architecture. Complementing, the Segment Anything Model (SAM) (Kirillov et al., 2023) for segmenting natural images, has also shown remarkable performance in medical imaging (Lee et al., 2024). Building on the success of foundation models, we previously developed the CellViT model (Hörst et al., 2024a), which combines ViT based foundation models with a segmentation head. Using this structure, we outperformed existing methods and achieved state-of-the-art (SOTA) results for cell detection and segmentation (Hörst et al., 2024a). The CellViT model has been validated in several independent studies. An adaption of CellViT, incorporating a tissue segmentation branch, won the Ocelot Challenge (Li et al., 2024). In CD20+ B cell quantification for lung tissue, CellViT effectively detected nuclei in CD20-stained sections, revealing associations between B cell clusters and granulomas in mice with M. tuberculosis infection (Koyuncu et al., 2024). CellViT also outperformed methods like StarDist and CellPose in analyzing acute lymphoblastic leukemia and

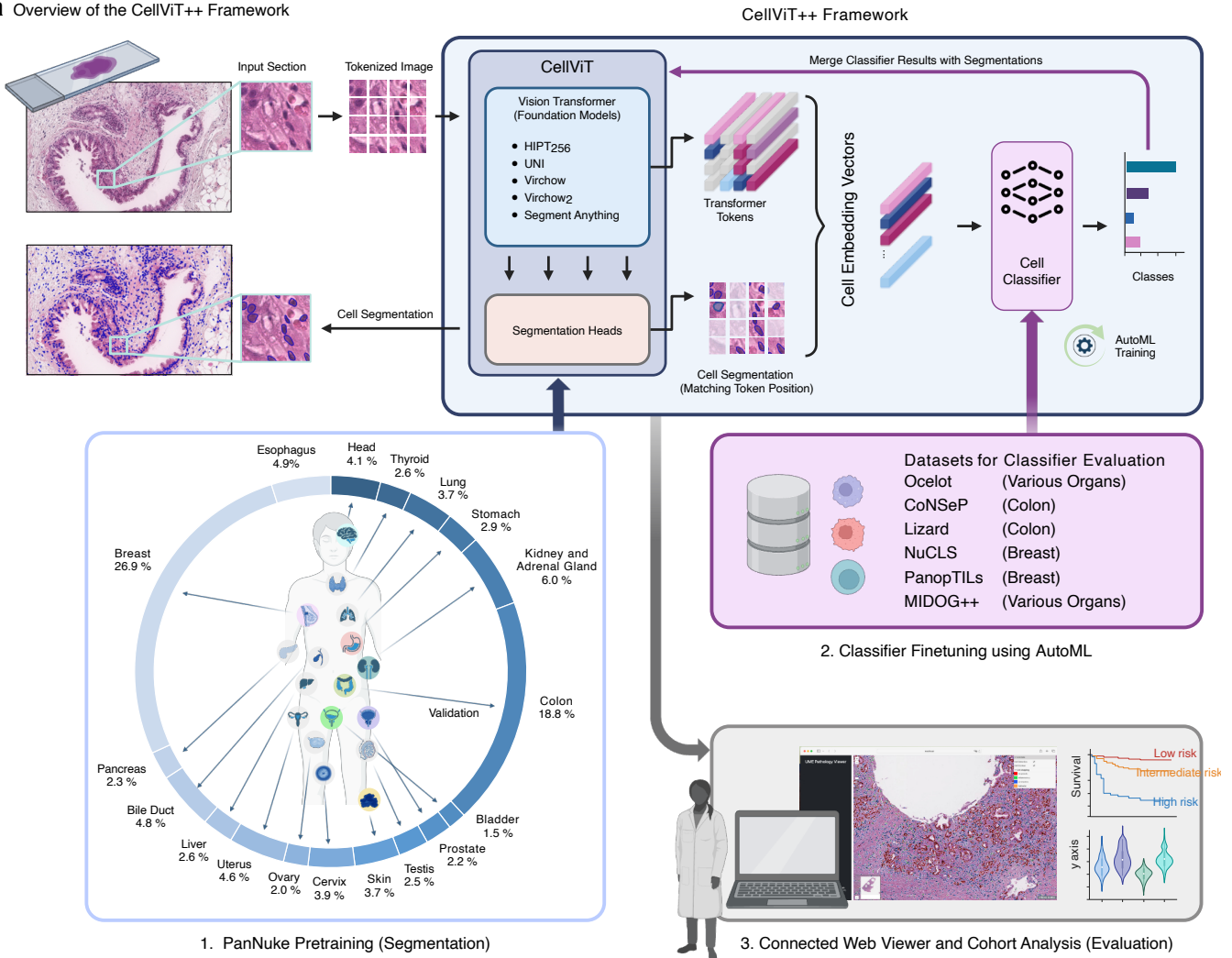
arXiv:2501.05269v1 [cs.CV] 9 Jan 2025

kidney samples (Raghaw et al., 2024; Guo et al., 2024). Additionally, applying CellViT to the HEST1K dataset (Jaume et al., 2024) demonstrates its ability to integrate molecular and morphological information, emphasizing the need for robust segmentation algorithms, as shown for the GATA3 concentration in heterogeneous cancer regions (Jaume et al., 2024).

Despite advancements in foundation models and cell segmentation algorithms, no model has yet demonstrated generalizability for arbitrary cell types or sufficient adaptability

without re-training. Current methods depend on extensive annotated datasets and precise segmentation masks. The PanNuke dataset, with 19 organ types and approximately 190,000 annotated cells, has been a valuable resource for cell segmentation but its utility is limited to the five specific cell types it includes: neoplastic, inflammatory, epithelial, connective, and dead cells. However, since different tissue and tumor types require diverse cell classification schemes, a dynamic adaptability in class assignment for detected cells is necessary. For instance,

a Overview of the CellViT++ Framework



b Automatically Derived Datasets from Registered HE and IF slides

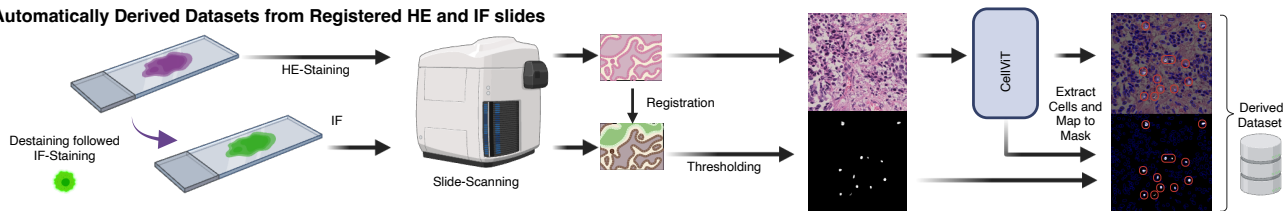


Fig. 1. Overview of the CellViT++ Framework. **a** Network architecture including the newly introduced cell classification module based on cell embeddings which are equal to the Transformer tokens of the last Transformer Block. Cell embedding vectors can be extracted in the forward pass in conjunction with the segmentation process. The embeddings are subsequently used to train a cell type classification module, to adapt the framework to new cell classes. The segmentation network of CellViT++ is pretrained using the PanNuke dataset (1). Tissue types highlighted in bold are selected for further analysis in this study. Subsequent classification modules are trained on unseen datasets (2) and the results are combined with the segmentation masks. Cohort analysis and image visualization can be performed with our web-based viewer (3). **b** Pipeline to automatically derive labels from registered H&E and IF scans using CellViT++, exemplified by the SegPath dataset.

the group of inflammatory cells encompasses various immune cell types, such as lymphocytes, neutrophils, eosinophils, and macrophages, with lymphocytes being particularly relevant in breast cancer prognosis (Sun et al., 2021; Liu et al., 2024). The standard approach for a new cell-class scheme is to create a corresponding dataset with several thousand annotated cells by pathologists to develop a model for the cell types of interest based on existing methods (Graham et al., 2019b; Stringer et al., 2021; Weigert & Schmidt, 2022). Creating expert-level cell segmentation annotations is more time-consuming and costly than creating a cell detection dataset without cell contours (Reiss et al., 2021), limiting new network candidates to detection-based models. An out-of-the-box algorithmic solution like the nnUNet for radiological images is still absent for digital pathology (Isensee et al., 2020).

To solve this problem, we propose CellViT⁺⁺, a framework designed for generalized cell segmentation in H&E-stained images (Fig. 1). Building upon the previously published CellViT architecture, our approach leverages the representation learning capacity of foundation models and the inherent structure of the Transformer architecture of the image encoder. During the forward pass through the CellViT model, deep cell features are computed alongside the segmentation masks without additional computational overhead (Fig. 1a). These cell embeddings are then used to build segmentation agnostic cell type classification modules to adapt the network to new cell types. This bypasses the traditional requirement for separate cell cropping and feature extraction stages seen in two-stage models (Huang et al., 2024). A key aspect of the CellViT⁺⁺ framework is the robust segmentation performance achieved by the segmentation heads, which allows us to focus solely on re-training the lightweight cell classification module to achieve accurate cell classification and segmentation across different cell types. We extend the original CellViT model by (1) incorporating several foundation models as image encoders, (2) extracting cell tokens for each detected cell, (3) introducing a lightweight cell classification module based on the cell tokens to swiftly adapt to new cell classification schemes, (4) optimizing the code for faster inference speed, and (5) providing an entire toolbox including a web-based visualization and annotation tool (Fig. 1a). To evaluate the efficiency of the classification approach, we show that integrating the classification modules at the bottleneck layer (last Transformer layer) of the encoder provides an effective method for adapting the model to new classes. We evaluate CellViT⁺⁺ using different foundation models as image encoders to assess their ability to generate discriminative cell embeddings. We included, in order of increasing parameter count, HIPT₂₅₆, UNI, Virchow₁, Virchow₂, as well as the domain-agnostic model Segment Anything Model (SAM-H). All CellViT⁺⁺ variants, respectively the segmentation models, have been pretrained on the heterogeneous PanNuke dataset (Fig. 1a). We utilize a wide range of cell datasets to test the cell classification module, including two multi-organ datasets (Ocelot (Ryu et al., 2023), MIDOG⁺⁺ (Aubreville et al., 2023)), that encompass organs not included in the PanNuke training data. Additionally, we assess CellViT’s performance on two common cancer types: breast cancer (NuCLS (Amgad et al., 2022), SegPath (Komura et al., 2023), PanopTILs (Liu et al., 2024)) and colorectal cancer (CoNSEP (Graham et al., 2019b), Lizard (Graham et al., 2021)) and compare our method with current baseline methods

on these datasets. Our method not only achieves outstanding performance but also yields remarkable results with significantly fewer samples while requiring substantially less energy resources (CO₂ equivalent) due to its efficient feature computation compared to all other methods.

Additionally, we also demonstrate that the CellViT⁺⁺ framework can achieve exceptional performance on unknown cell types without the need for pathologist-curated datasets. We employ the SegPath dataset (Komura et al., 2023), which includes registered pairs of H&E and immunofluorescent (IF) stainings from the same tissue sections. The IF stainings, which use specific antibodies tagged with fluorescent markers to highlight cellular components, enable the automatic generation of segmentation masks for the corresponding H&E sections through thresholding techniques. Although these masks initially lack instance-level segmentations, the CellViT⁺⁺ model can detect and segment single cells in the H&E samples and transfer these segmentations to the IF masks. This approach facilitates the creation of large-scale cell datasets without needing expert pathologist annotations. A schematic of this method is illustrated in Fig. 1b. We exemplify this approach by generating datasets for lymphocytes and plasma cells in breast tissue. Classifiers trained on these automatically generated datasets achieved nearly the same performance as those trained on pathologist-annotated datasets for lymphocytes and even surpass them for plasma cells.

To democratize the use of CellViT⁺⁺ as a high-throughput pipeline, we have developed and released it as an open-source toolbox that does not require specialized high-performance computing clusters or coding expertise. The toolbox automates hyperparameter tuning, functioning as a type of AutoML tool (Waring et al., 2020). Additionally, we provide a new lightweight, web-based WSI viewer for visualizing detection/segmentation results, which offers greater accessibility and ease of use compared to traditional local software solutions. To minimize annotation efforts for pathologists, the toolbox includes a web-based annotation tool that facilitates quick reclassification and relabeling for cells. All trained classification modules are integrated into our framework and can be used out of the box. The toolbox is available at <https://github.com/TIO-IKIM/CellViT-plus-plus>. To avoid confusion, CellViT refers to the segmentation model from our previous work, pretrained exclusively on PanNuke, while CellViT⁺⁺ denotes the new framework introduced in this study, which integrates the pretrained CellViT model with a cell classification module.

Results

PanNuke Pretraining Results

A fundamental component of our framework is the pretraining of the segmentation models on the PanNuke dataset, which contains 190,000 extensively annotated cells across 19 tissue types. These pretrained models (CellViT) are then integrated into the CellViT⁺⁺ framework without further modification. Before evaluating the CellViT⁺⁺ framework, it is essential to demonstrate that the segmentation models achieve satisfactory performance. To this end, we evaluated all models using the official 3-fold cross-validation (CV) split of the PanNuke dataset (Gamper et al., 2020). The primary metric employed

¹Corresponding Author: fabian.hoerst@uk-essen.de

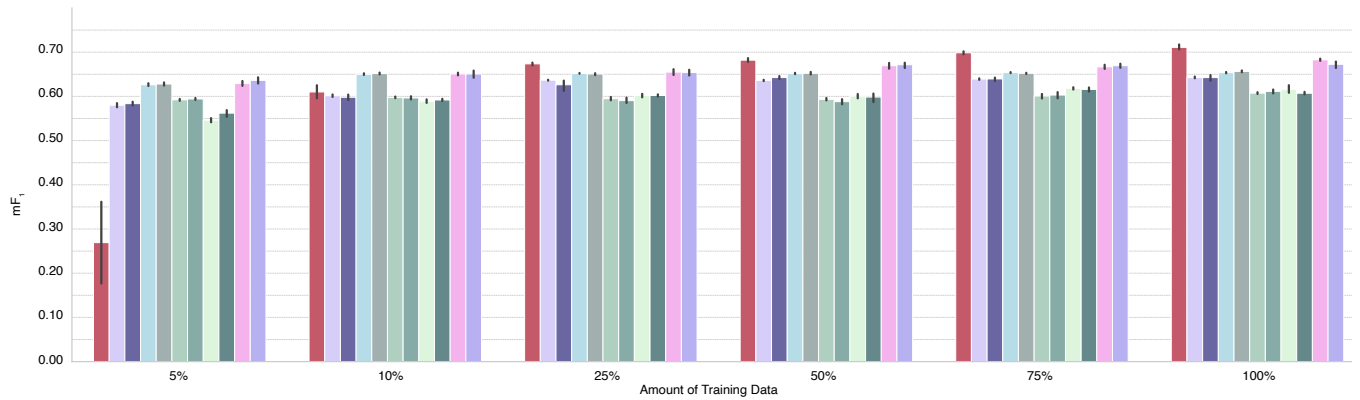
is the mean Panoptic Quality (mPQ), as it combines segmentation and detection performance into a single score while also considering cell classes. In addition to the already published CellViT_{H IPT256} and CellViT_{SAM-H} models, we included three additional histopathological foundation models (UNI, Virchow, and Virchow₂). The results reveal that all CellViT variants with a foundation model encoder exhibited superior performance compared to the baseline model CellViT_{ViT-S} (vanilla ViT small) with an average improvement of at least 7.45% over the baseline (CellViT-ViT_s : 0.4417 mPQ, Standard Deviation (SD) 0.0500 vs. CellViT-HIPT₂₅₆ : 0.4846 mPQ, SD 0.0503). Among the evaluated models, the Segment Anything Model (CellViT_{SAM-H}) achieved the highest performance with 0.49803 mPQ (SD 0.041), benefiting from its extensive segmentation pretraining task. A full overview about all results are given in the [Extended Data Fig. 1a](#). While all models showed promising cell detection and segmentation results, our subsequent analyses will focus on identifying the encoder yielding the most generalistic cell representations. All subsequent CellViT segmentation models included in the CellViT⁺⁺ framework have been pretrained on 95% patches

of the PanNuke dataset, with the remaining 5% used to detect overfitting. If not otherwise stated, each cell classification module consists of one hidden layer with ReLU activation function. As illustrated in Fig. 1a, we assigned each identified cell the corresponding token of the ViT-based image encoder, and trained the classifier solely based on the tokens.

Data-Efficient Cancer Cell Detection Across Multiple Organs Using CellViT⁺⁺

Although the PanNuke dataset encompasses a multitude of organs and includes the cell category neoplastic cells, differentiating malignant and benign cells within the neoplastic cell group is a key objective in routine histopathological diagnostics. The Ocelot dataset contains a total of 71,691 malignant tumor cells and 41,335 non-tumor cells annotated in 663 $num_{1024} \times num_{1024}$ pixel (px) image sections including six human organs, namely bladder, endometrium, head/neck, kidney, prostate, and stomach (see [Extended Data Fig. 1c](#)). To obtain the mean and standard deviation, each experiment was repeated five times on the train and validation split, with evaluation on the official test set. The metric utilized is the mean F₁-score (mF₁). The dataset also includes area

a Ocelot Test Scores Across all Organs for Ascending Training Dataset Size



b Organ-wise Comparison

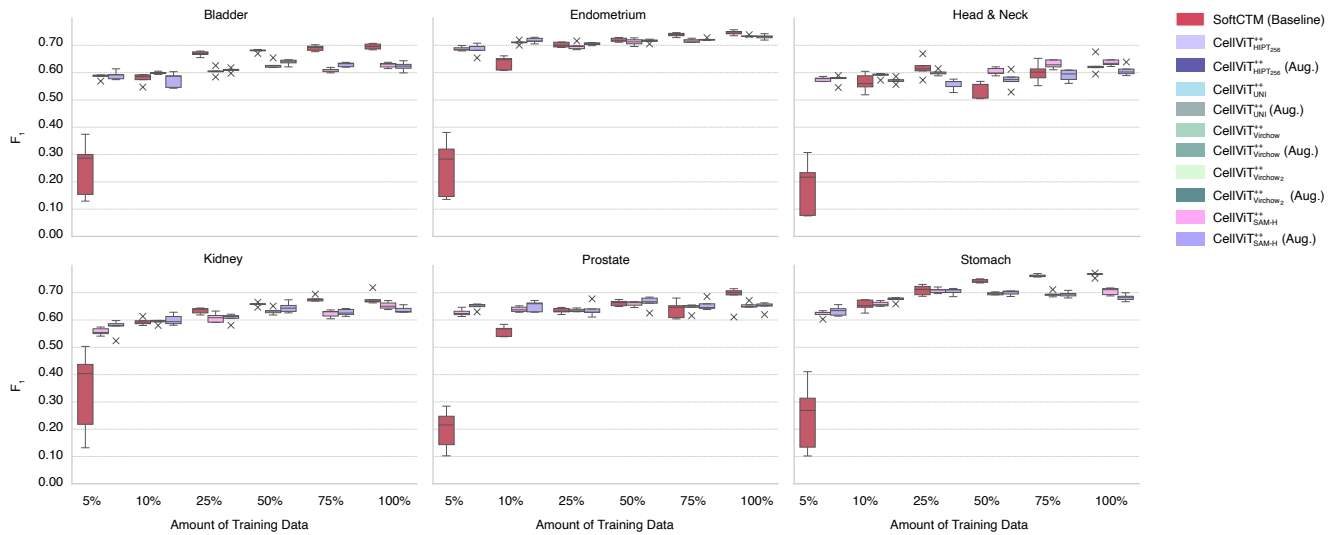


Fig. 2. Ocelot results and comparison with state-of-the-art baseline network SoftCTM. a Mean F₁-Score averaged over all tissue types in the dataset on the official test set for multiple image encoders. Each cell classification module and the baseline SoftCTM model were trained on a limited amount of training data. Results are given for 5 experiments with different seeds. **b** Organ-wise detection results of the baseline SoftCTM model in comparison to the best performing CellViT⁺⁺ model, again trained on limited dataset sizes.

segmentations of tumor tissue, intended to serve as an additional aid for cell classification. Only the subset containing cell annotations is utilized in this current study. As demonstrated by Li et al. (2024), the combination of CellViT with a tumor segmentation model (ensemble) currently yielded SOTA results with a mF_1 -score of 0.7243 on this data set. Other comparative methods include a ResNet ensemble by Lafarge & Koelzer (2024) (0.6617 mF_1), the FC-HardNet model (0.6992 mF_1) (Lo & Yang, 2024), and the model by Millward et al. (2024) (0.7221 mF_1). All these models consist of at least two models for cell and tissue segmentation followed by a merging strategy to fuse tissue segmentations with the cell segmentations. In contrast, the cell-only baseline just reached 0.6444 mF_1 (Ryu et al., 2023).

For comparison with our model, we used the CNN-based SoftCTM model (tissue and cell), which has been externally validated and reported to achieve a performance of 0.7172 mF_1 -score. We selected this architecture because it does not rely on CellViT as a cell segmentation model. We retrained the SoftCTM model five times and report the average results along with the standard deviation. On the external test set, SoftCTM achieved 0.7109 mF_1 (SD 0.0069), while the best CellViT⁺⁺ variant (CellViT⁺⁺_{SAM-H}) achieved 0.6827 mF_1 (SD 0.0028). The results are particularly noteworthy as CellViT⁺⁺_{SAM-H} outperformed the cell-only baseline (0.6444 mF_1) by $\Delta = +0.0383$ mF_1 , despite the fact that only the cell classification module, and not the segmentation model, was re-trained. Furthermore, as a cell-only model, CellViT⁺⁺_{SAM-H} yielded a performance close to the supervised baseline of SoftCTM ($\Delta = -0.0282$ mF_1), which utilized additional tumor-microenvironment tissue context. In contrast, all models using histopathological foundation model encoders performed inferior to the CellViT⁺⁺_{SAM-H} model. A table with all results can be found in the Supplement (Table S5).

Data augmentation is a common regularization technique to enhance the generalizability and performance of an algorithm. To evaluate its impact, we augmented the input patches using common augmentation techniques (see Supplementary Table S20). The results, given in Fig. 2a, indicate that data augmentation has a negligible effect on classification performance, with marginal improvements for CellViT⁺⁺_{UNI} ($\Delta = +0.0028$ mF_1) and CellViT⁺⁺_{Virchow} ($\Delta = +0.0040$ mF_1), but reduced performance for CellViT⁺⁺_{Virchow2} ($\Delta = -0.0087$ mF_1) and CellViT⁺⁺_{UNI} ($\Delta = -0.0101$ mF_1).

Given the challenge of acquiring labeled WSI data and the difficulty of obtaining thousands of annotated cells with expert-level precision, we also investigated the data efficiency. We sequentially sampled subsets of the training data, comprising 5%, 10%, 25%, 50%, and 75% of the training dataset (see S3 in the Supplement for dataset overview). The results, illustrated in Fig. 2a and 2b, demonstrate that all CellViT⁺⁺ variants achieved significantly better performance with only 5% of the data compared to the reference method. At least 25% of the training data were necessary (equals to 18,573 cells) such that SoftCTM was on par. In contrast, the performance of the CellViT⁺⁺ models saturated, with a tripling of the training dataset size resulting in only a modest increase in F_1 -score for CellViT⁺⁺_{SAM-H} (25% data 0.6550 mF_1 , SD 0.0073 vs. 75% data with 0.6669 mF_1 , SD 0.0054). Additionally, the comparison reveals that the HIPT₂₅₆, UNI, and SAM-H variants generated embeddings that allow for competitive classification perfor-

mance, whereas the models of the Virchow series (Virchow, Virchow₂) consistently yielded inferior results on this dataset. There is no demonstrable benefit from using data augmentation even when training data is limited. Additional results for the CellViT⁺⁺_{SAM-H} model, along with SoftCTM, are shown in Fig. 2b, stratified by tissue type. The box plots indicate that CellViT⁺⁺ achieved better and more stable performance with limited training data, as the segmentation decoder serves as a strong backbone for cell detection. For underrepresented tissue types in the Ocelot dataset, such as head and neck, CellViT⁺⁺ performed comparably or better than SoftCTM even with all available training data (e.g., Head/Neck: SoftCTM 0.6267 mF_1 , SD 0.0268 vs. CellViT⁺⁺_{SAM-H} 0.6359 mF_1 , SD 0.0095). These results highlight the exceptional data efficiency of our algorithm, making it particularly well-suited for exploratory analysis and establishing a strong benchmark in low-data regimes. A detailed breakdown is provided in the Supplementary Table S4.

Data Efficient Learning for Cell Classification in Colorectal Cancer

Colorectal cancer (CRC) is the third most common malignancy worldwide and a leading cause of cancer-related mortality, with global cases projected to rise from 1.9 million in 2020 to 3.2 million by 2040, and deaths expected to increase from 0.9 million to 1.6 million over the same period (Klimeck et al., 2023; World Health Organization: Regional Office for Europe, 2020). Enhanced segmentation models support research efforts by providing a deeper understanding of the tumor microenvironment, ultimately aiding in the development of more targeted and effective therapeutic strategies.

Recent releases of two comprehensive datasets, CoNSEP and Lizard, have significantly advanced the field by providing extensive cell annotations and segmentation masks. These resources serve as crucial benchmarks for developing and validating cell segmentation models in colorectal cancer research. The CoNSEP dataset includes 41 annotated tiles with a size of $1,000 \times 1,000$ px from University Hospitals Coventry and Warwickshire, UK, comprising a total of 24,332 cells divided into a fixed training set (15,555 cells) and test set (8,777 cells), as shown in the Extended Data Fig. 1d. The cells are categorized into four classes: inflammatory cells, epithelial cells, spindle-shaped cells, and miscellaneous cells. According to Graham et al. (2019b), we followed the official split using 27 tiles for training and 14 for testing. A 5-fold CV strategy was employed on the training slides to assess mean model performance.

We compare CellViT⁺⁺ with the original HoVer-Net publication, a self-trained HoVer-Net model, and the PointNu-Net (Yao et al., 2023), the current SOTA network on this dataset. The evaluation metrics includes the mPQ+ score, a variant of the mPQ score for multiclass cell segmentation, as well as the binary F_1 (binary cell detection) and Dice score (binary cell segmentation). Among all CellViT⁺⁺ variants, the SAM-H model performed best, achieving an mPQ+ of 0.461 (SD 0.014). The baseline models achieved 0.429 mPQ+, (HoVer-Net), and 0.446 mPQ+ (PointNu-Net). In terms of mPQ+, we set a new benchmark with CellViT⁺⁺_{SAM-H}.

In a zero-shot evaluation setting using models pretrained on the PanNuke dataset (without cell classification module), HoVer-Net achieved an F_1 -score of 0.691 and a Dice score of 0.802. In comparison, CellViT⁺⁺_{SAM-H} reached an F_1 -score of

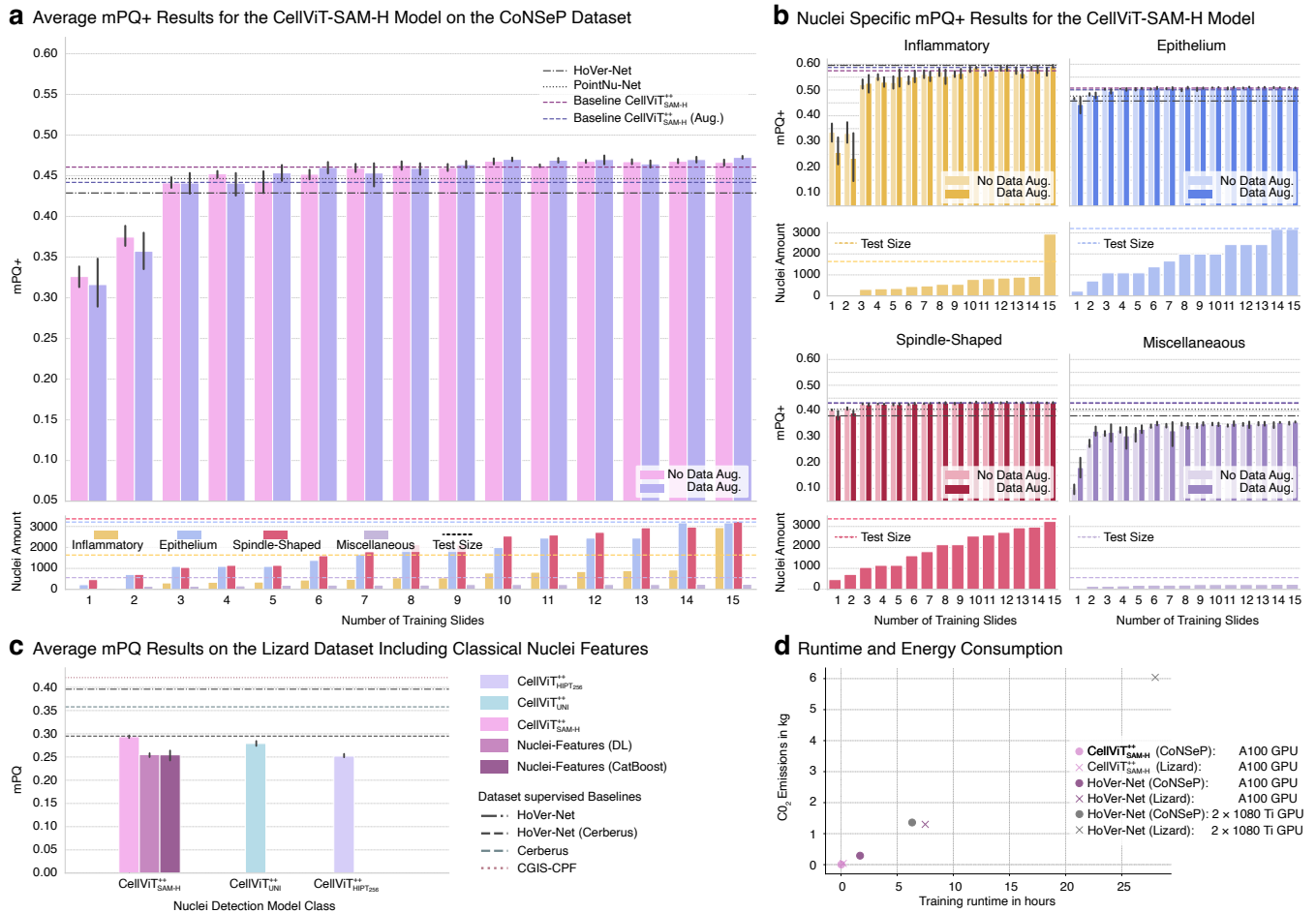


Fig. 3. Experimental evaluation on colon tissue cell datasets. **a** Performance comparison of the CellViT⁺⁺_{SAM-H} network, with and without data augmentation, across varying amounts of training slides, besides baseline results from HoVer-Net and PointNu-Net (SOTA) on the CoNSEp dataset. The upper panel presents the mean panoptic quality (mPQ), while the lower panel depicts the number of nuclei in the datasets. Training data is incrementally increased from a single crop of 1 slide to 15 crops across 15 slides. **b** Nuclei specific performance comparison on CoNSEp. **c** Average mPQ on the Lizard dataset compared to top-performing networks. Additionally, CellViT⁺⁺_{SAM-H} is evaluated using both ViT token embeddings as cell features and classical nuclei features with deep learning and CatBoost classifiers. The HoVer-Net Cerberus is a re-trained version by Graham et al. (2023). **d** Runtime and energy efficiency comparison of our network, trained on the CoNSEp and Lizard datasets, against HoVer-Net.

0.772 and a Dice score of 0.845, demonstrating remarkable zero-shot performance. A detailed overview of the results for all CellViT⁺⁺ models and the comparison methods is provided in Supplementary Table S8.

To further explore data efficiency, we simulated an active labeling approach, incrementally increasing the number of training tiles, starting with just one. Tiles were selected to ensure a balanced representation of cell classes. We repeated the experiments five times, without cross-validation, both with and without data augmentation. Remarkably, using only three fully annotated tiles with approximately 2,500 cells, CellViT⁺⁺ achieved performance comparable to the PointNu-Net network (trained on 27 tiles), and with four tiles, we exceeded it (see Fig. 3a). The analysis by cell class presented in Fig. 3b supports this hypothesis, demonstrating that careful selection of regions of interest (ROIs) with diverse cell composition and distinct cell nuclei can produce robust results even with limited data. For example, increasing the number of annotated inflammatory cells beyond 750 showed minimal impact, and a similar plateau effect was observed for epithelial and spindle-shaped cells. Our results on the CoNSEp dataset confirm that data

augmentation does not improve performance and, in some cases, may reduce it (see Fig. 3a and 3b for inflammatory cells). This finding aligns with the analyses on the Ocelot dataset. In conclusion, we achieved superior performance in cell classification and excellent zero-shot segmentation on the CoNSEp dataset. Due to the excellent performance of CellViT⁺⁺_{HPT256}, CellViT⁺⁺_{UNI}, and CellViT⁺⁺_{SAM-H}, we focus our analysis on these networks to evaluate which network yields to most representative cell embeddings.

Slide Resolution Generalizability

Variability in lab protocols and scanning devices results in WSIs being acquired at different resolutions than the CellViT⁺⁺ training standard of 0.25 $\mu\text{m}/\text{px}$. Consequently, it is crucial to validate CellViT⁺⁺ across a range of image resolutions. For this purpose, we employed the Lizard dataset, which provides ROIs from colorectal cancer samples at a resolution of 0.50 $\mu\text{m}/\text{px}$. This dataset is among the largest available, featuring over 418,000 cell segmentation masks categorized into epithelium, lymphocytes, plasma cells, neutrophils, eosinophils, and connective tissue cells (see Extended Data Fig. 1d, and Supplementary Table S7). In a previous study,

we observed that directly applying $0.50 \mu\text{m}/\text{px}$ without pre-processing image resolutions resulted in a significant distribution shift (Hörst et al., 2024a), degrading performance. To mitigate this issue, we applied a resampling method using a Lanczos filter to upscale the images to $0.25 \mu\text{m}/\text{px}$, process them with CellViT⁺⁺, and then downscale the segmentation masks back to $0.50 \mu\text{m}/\text{px}$. We compare the performance of CellViT⁺⁺ with resampling to several other segmentation models specifically tailored for this dataset, including HoVer-Net, Cerberus (Graham et al., 2023), and CGIS-CPF (Zhong et al., 2023). These models were trained directly on the Lizard dataset without any resampling or resolution adaptation. For evaluation, we use the PQ metric and report the average 3-fold CV results including standard deviation. We note that we removed the PanNuke samples of the Lizard dataset in our experiments, as they have been used in pretraining the CellViT⁺⁺ segmentation models. The best CellViT⁺⁺ model with SAM-H encoder achieved a binary PQ score of 0.536 (SD 0.009), which is lower than of the comparison methods (HoVer-Net-Cerberus: 0.584 (SD 0.014), HoVer-Net-Baseline: 0.624 (SD 0.139), Cerberus: 0.612 (SD 0.009), CGIS-CPF: 0.660 (SD 0.009)). Incorporating the token-based cell classification module led to a mPQ-score of 0.294 (SD 0.002), which comes close to the performance of the supervised models with scores between 0.295 (SD 0.018) for HoVer-Net (Cerberus) and 0.421 (SD 0.013) for CGIS-CPF. These results highlight two key points: Even though CellViT⁺⁺ was developed and optimized for a resolution of $0.25 \mu\text{m}/\text{px}$, it showcases remarkable adaptability across different resolutions, whereas the models evaluated here were trained directly on the Lizard dataset with resolution of $0.50 \mu\text{m}/\text{px}$. Secondly, CellViT⁺⁺'s approach of utilizing a pre-trained segmentation network in a zero-shot setting, while only fine-tuning the classifier, offers a unique advantage in scenarios where annotated data may be limited or expensive to obtain. This efficient transfer learning strategy contrasts with the more data-intensive approach of training models from scratch, which, while beneficial for the baseline models in this specific case, may not always be feasible or desirable in real-world applications.

Comparison with Conventional Feature Engineering Approaches

To address the performance gap observed between CellViT⁺⁺ and supervised models on the Lizard dataset, we examined if the quality of our token embeddings contributed to the discrepancy. For this, we compared the CellViT⁺⁺ embeddings of HIPT₂₅₆, UNI and SAM-H image encoder with conventional handcrafted cell features (histomics). For each cell identified by CellViT⁺⁺_{SAM-H}, we extracted 128 pre-defined nuclear features (Huang et al., 2024) (e.g., color, texture, shape, spatial, morphology, orientation) and trained a classifier similar to the token based classification module, as well as various classical machine learning models, including SVMs and CatBoost. The results, depicted in Fig. 3c, reveal that deep learning features led to an mPQ score of 0.294 (SD 0.002), while handcrafted features with a deep learning classifier scored 0.255 (SD 0.002). The best classical machine learning model (CatBoost) using these handcrafted features achieved an mPQ of 0.255 (SD 0.009), all lower than the foundation models cell features of CellViT⁺⁺_{SAM-H} and CellViT⁺⁺_{UNI} (0.279 mPQ, SD 0.004), but on par with CellViT⁺⁺_{HIPT₂₅₆} (0.252 mPQ, SD 0.003). These findings demonstrate that the token embed-

dings from CellViT⁺⁺ are generally more informative than traditional handcrafted histomics features and remove human bias. Furthermore, generating token embeddings is more computationally efficient, as it avoids the additional overhead of calculating Histomics features, which took an average of 18.71 ± 37.55 ms per cell, contributing to a substantial time cost. More results are given in the Supplement (Tables S6-S10).

Characterization of the Tumor Microenvironment in Breast Cancer

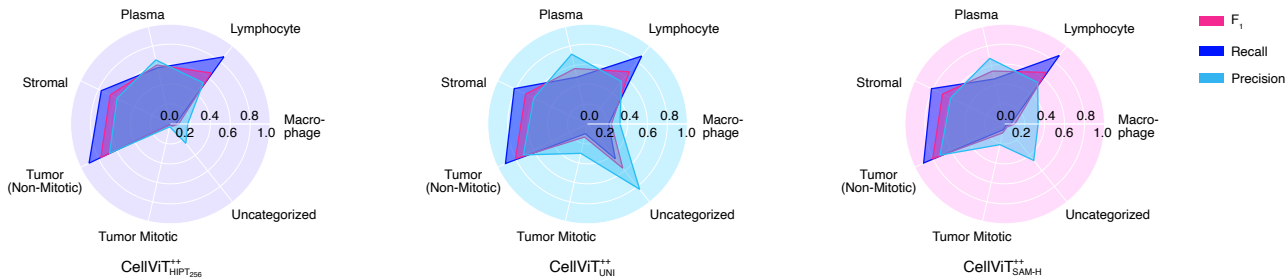
Among various cancer types, breast cancer is notably significant as the most frequently diagnosed cancer among women (World Health Organization: Regional Office for Europe, 2020). For research on this tumor type, two complementary cell datasets have been released: the NuCLS dataset and the PanopTILs dataset. The NuCLS dataset includes multiple classification levels to distinguish between tumor cells, stromal cells, and inflammatory cells, while the PanopTILs dataset is specifically designed to assess tumor-infiltrating lymphocytes (TILs) and additional cellular components within the tumor microenvironment. Tumor-infiltrating lymphocytes are a critical component of the immune response within the tumor microenvironment and have been shown to correlate with patient prognosis and response to immunotherapy in several cancer types, including breast cancer (Sun et al., 2021). Due to the novelty of these datasets, advanced network architectures beyond Mask R-CNN models have yet to be developed. In this study, we establish a robust baseline on both the NuCLS (see Fig. 4a) and PanopTILs datasets (see Fig. 4b). Our analysis of F₁, recall, and precision scores for the CellViT⁺⁺ models on NuCLS showed strong overall performance (see Fig. 4a). However, for rare cell types such as macrophages and mitotic tumor cells, recall is lower while precision is higher. This suggests that although these cells are identified less frequently, when they are detected, the detections are more accurate. In line with this, our models demonstrated strong performance on the PanopTILs dataset, achieving high F₁-scores for TILs (CellViT⁺⁺_{SAM-H}: 0.801 F₁, SD 0.006). Additionally, for epithelial cells we achieved consistent F₁-scores of 0.800, and for stromal cells of 0.643, as depicted in Fig.4b). We anticipate that releasing these models will facilitate quantitative analysis of the tumor microenvironment in breast cancer tissue, replacing manual counting in ROIs by pathologists with automated methods (Salgado et al., 2015; Amgad et al., 2020).

Reducing CO₂ Emissions and Training Time through Energy-Efficient Fine-tuning

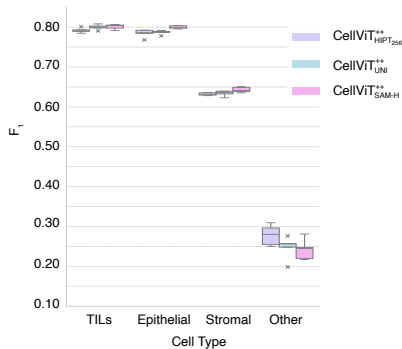
Training large models typically demands considerable computational resources, leading to significant CO₂ emissions (Patterson et al., 2021). Our method mitigates this issue by utilizing pretrained domain-specific segmentation models, enabling efficient fine-tuning on new tasks and thereby reducing the carbon footprint associated with model training. We evaluate the energy efficiency of our approach using the metrics from Lacombe et al. (2019). Compared to traditional models such as HoVer-Net, our method demonstrated substantial reductions in both training time and CO₂ emissions. For instance, training HoVer-Net on the CoNSeP dataset with two Nvidia 1080 Ti GPUs took 6.33 hours, and 27.98 hours for the Lizard dataset, with an estimated power consumption of 3,170 WH and 14,000 WH, respectively.

To reduce training runtime, we performed experiments with

a CellViT Results on the NuCLS Dataset



b CellViT Results on the PanopTILs Dataset



c NuCLS Test Results with Networks Trained on Data from Registered HE and IHC Slides

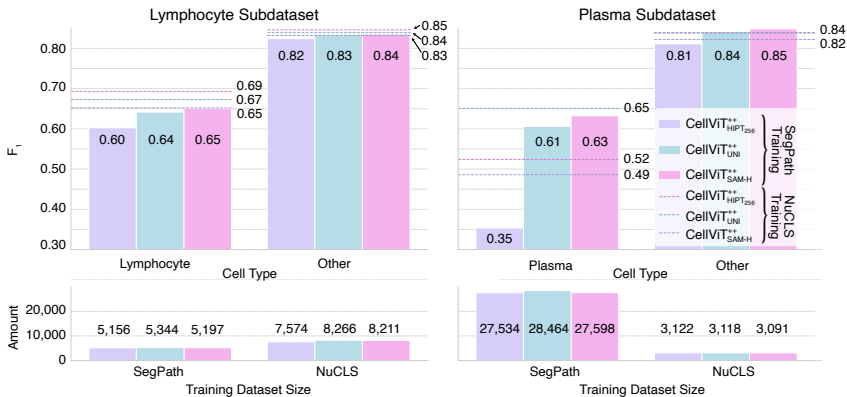


Fig. 4. Experimental evaluation on breast cancer tissue datasets, including training on automatically derived lymphocytes and plasma cells from the SegPath dataset. **a** Comparison of F_1 -score, precision, and recall for different CellViT⁺⁺ models on the NuCLS dataset with all cell types included. **b** CellViT⁺⁺ performance on the PanopTILs dataset for analyzing the tumor microenvironment in breast cancer. **c** Detection performance comparison of our network on the NuCLS test set, trained with automatically derived cells from the SegPath dataset versus fully supervised training on the NuCLS training dataset for lymphocytes and plasma cells. The lower panel shows the number of training cells in both datasets. For SegPath, CellViT⁺⁺ was applied to HE-slides, with the resulting cell contours mapped to the IHC mask to derive cell classes.

an Nvidia A100 GPU, which reduced the training times to 1.70 hours (680 WH) and 7.5 hours (3,000 WH) for both datasets (see Fig. 3d). Our CellViT⁺⁺ model, on the other hand, required only 81 seconds for training on the CoNSEP (9.23 WH) and 12 minutes for training on the Lizard dataset (92.16 WH). Figure 3d illustrates the superior resource efficiency, highlighting lower training times and CO₂ emissions compared to HoVer-Net on various hardware and datasets. Even with a hyperparameter search involving 100 runs, our CO₂ footprint remained lower than that of HoVer-Net. This efficiency arises because approximately 90% of the training time in our AutoML pipeline is devoted to the initial caching of CellViT⁺⁺ results and cell tokens. Once this step is completed, hyperparameter tuning becomes inexpensive, provided that data augmentation is not employed. In contrast, methods requiring full training of a segmentation model for each experiment incur higher computational and environmental costs.

Automated Cell Dataset Generation from IF Stainings: Reducing Pathologist Involvement

Our previous analyses have demonstrated that models like HoVer-Net and SoftCTM require large datasets with precise segmentation masks to achieve optimal performance, which creation is often performed from or at least supervised by pathologists. Manual annotation, particularly of segmentation masks, is resource-intensive and costly, posing a significant bottleneck in translational research. This limitation makes it

impractical to create datasets at the necessary scale. Automated generation of cell datasets from IF staining presents a promising approach to reduce the reliance on pathologists for fine-grained segmentation annotations.

To address this challenge, we propose an automated workflow for generating cell-specific datasets with minimal manual intervention. In this method, tissue samples are initially stained with H&E, then destained and subsequently re-stained using immunohistochemistry (IHC) or IF markers to specifically target the desired cell types. After scanning the H&E and IHC/IF samples, cell-level registration is performed to align the images, and a binary mask of positively stained cells is created through thresholding of the IF channel. A CellViT⁺⁺ model is then applied to the H&E-stained images, to extract cell segmentation masks. These mask can be re-mapped to the registered IF masks, marking positive and negative cells. The whole dataset creation workflow is depicted in Fig. 1b. This approach significantly reduces the need for manual annotation, requiring only a small pathologist-approved validation set to ensure accuracy. In this study, we demonstrate the method using two exemplar cohorts from the SegPath dataset (Komura et al., 2023), focusing on breast tissue. The dataset employs CD3/CD20 IF staining to specifically identify lymphocytes and MIST1 staining to highlight plasma cells along with registered H&E slides. Training was conducted on cells automatically extracted from this dataset, following the previously described strategy. Final validation of the classifiers was performed on the pathologist-approved subset of the NuCLS

dataset, in a one-vs.-all setting (lymphocytes/plasma cells vs. all other types). As baselines, we additionally trained lymphocyte and plasma cell classifiers on the NuCLS training dataset. We successfully extracted around 5,000 lymphocytes and over 27,000 plasma cells from the SegPath dataset (see Fig. 4c). In comparison, the NuCLS training dataset contained approximately 7,500 lymphocytes and around 3,000 plasma cells. For training on the automatically generated cell datasets, the CellViT⁺⁺_{SAM-H} model achieved an F₁-score of 0.651 for the detection of lymphocytes and 0.632 for plasma cells. In contrast, training on the NuCLS dataset resulted in an F₁-score of 0.693 (-0.042) for lymphocytes and 0.524 (+0.108) for plasma cells (see Fig 4c). Notably, we trained a classifier for plasma cells using CellViT⁺⁺_{UNI} tokens on the NuCLS data, achieving an F₁-score of 0.651, slightly surpassing the results obtained with our automatically generated dataset. On average, the performance of classification modules trained on the automatically generated SegPath cell dataset approached that of those trained on the expert-level annotated NuCLS datasets (lymphocytes) and, with a sufficient amount of annotated cell data, even exceeded it (plasma cells).

Dealing with Low Prevalence when Detecting Mitotic Figures

As demonstrated on the NuCLS dataset, recall for rare cell types, such as mitotic figures, is often low, while precision tends to be higher. To further evaluate this effect, we applied CellViT⁺⁺ to mitosis detection using the MIDOG++ dataset (Aubreville et al., 2023), which includes human and canine tissue samples. The MIDOG++ dataset presents a challenging task due to the scarcity of mitotic figures, comprising only 0.16% of the cell population. It contains 11,937 annotated mitotic figures and 14,351 hard negatives (non-mitotic figures that could falsely be recognized as mitotic figures) across 503 tissue sections. Notably, the dataset is partially annotated, with non-mitotic cells left unannotated unless labeled as hard negatives. For dataset preparation, we extracted all cells using CellViT and labelled them as either mitotic or non-mitotic. This resulted in a dataset of 7,398,795 cells, used for CellViT⁺⁺_{SAM-H} training. Given the extreme class imbalance, we adjusted the training data to include mitotic to non-mitotic cell ratios of 1:1, 1:20, and 1:200. The results are presented in Table 1. Our findings indicate that the model with 200 additional non-mitotic cells per mitotic figure performs best. A detailed analysis of the precision and recall scores (Supplementary Tables S17 and S18) confirms that for rare events such as mitosis, recall remained lower than precision. On average, the model achieved a precision of 0.66 (SD 0.14), which is higher than the recall of 0.54 (SD 0.09). Performance also varies by tissue: for example, in human melanoma, the model reached a precision of 0.83 (SD 0.03) and a recall of 0.62 (SD 0.03), whereas in human breast cancer tissue, the precision was 0.77 (SD 0.04) and the recall 0.49 (SD 0.03). Despite the applicability of our approach, it falls short of the baseline detection model RetinaNet. Although our cell classification module had an F₁-score of 0.998 on the validation dataset, its performance degraded when applied at the WSI level due to the large number of cells evaluated. This degradation occurs because even a small false positive rate or a small amount of missed mitotic figures can lead to a significant number of misclassifications when applied to million of cells. A visualization is given in Extended Data Fig. 3.

Table 1. Results (F₁) on the MIDOG++ test dataset, categorized by organ and sample origin. For the CellViT⁺⁺ models, we also incorporated additional non-annotated cells to enhance the distinction between mitotic and non-mitotic cells during training. Specifically, 0, 20, or 200 (ratios 1:1, 1:20 and 1:200) additional non-mitotic figures were added per annotated mitotic figure.

Models		RetinaNet	CellViT ⁺⁺ _{SAM-H}		
Organs	Origin	Baseline	Ratio 1:1	Ratio 1:20	Ratio 1:200
Breast Cancer	Human	0.71 (SD 0.02)	0.50 (SD 0.01)	0.55 (SD 0.01)	0.60 (SD 0.01)
Neuroendocrine Tumor		0.59 (SD 0.01)	0.36 (SD 0.08)	0.45 (SD 0.02)	0.50 (SD 0.00)
Melanoma		0.81 (SD 0.01)	0.61 (SD 0.09)	0.67 (SD 0.03)	0.71 (SD 0.02)
Cutaneous Mast Cell	Canine	0.82 (SD 0.01)	0.63 (SD 0.03)	0.66 (SD 0.02)	0.70 (SD 0.01)
Lung Cancer		0.68 (SD 0.02)	0.34 (SD 0.03)	0.41 (SD 0.01)	0.43 (SD 0.02)
Lymphoma		0.73 (SD 0.01)	0.47 (SD 0.04)	0.51 (SD 0.01)	0.58 (SD 0.01)
Soft Tissue Sarcoma		0.69 (SD 0.01)	0.53 (SD 0.04)	0.53 (SD 0.01)	0.57 (SD 0.02)

Discussion

Current approaches for cell segmentation and classification in digital pathology rely on large, fine-grained annotated datasets and precise segmentation masks, which are both cost- and time-intensive to acquire. Additionally, different tissue and tumor types require distinct cell classification schemes (e.g., TILs instead of generic inflammatory cells), adding further complexity. Traditional methods are limited in their generalizability and lack flexibility for re-training and adaptation. This limitation necessitates the creation of a new dataset for each application, followed by the training of models such as HoVer-Net or SoftCTM, which is again resource-intensive and time-consuming.

The key innovation of our work is the development of CellViT⁺⁺, a generalized framework for cell segmentation in H&E images that allows lightweight adaptability without computational overhead. In our approach, deep cell features are extracted directly alongside segmentation masks, allowing for the creation of cell classification modules for new classification schemes without the need for re-training the segmentation model. CellViT⁺⁺ does not require data augmentation, which permits caching of cell segmentations and features during the first epoch of our AutoML hyperparameter search, further accelerating the training process. This feature is particularly beneficial for hyperparameter tuning, as caching only needs to be performed once per dataset.

To evaluate the effectiveness of the CellViT⁺⁺ framework, we conducted a series of experiments using datasets with varying properties, including differences in scanning resolution, tissue type, hospital origin, scanning devices, and cell types. Parts of our study focused on the clinically relevant cancer types colorectal cancer and breast cancer, both of which have high incidence and mortality rates, posing substantial challenges to healthcare systems worldwide. Our approach excels in scenarios with limited labeled data, highlighting its suitability for low-data environments. Importantly, the segmentation decoders in CellViT⁺⁺ were not fine-tuned in this study, demonstrating its robust zero-shot segmentation capabilities and efficient classification performance, even when confronted with new cell types or tissues not represented in the training data. The versatility of our model suggests that it is a suitable foundational tool for future research. We envision significant applications, particularly in the discovery and validation of biomarkers, by providing adaptable and precise cellular features for in-depth cohort analysis. The deep cell features extracted from various tissue samples can enhance

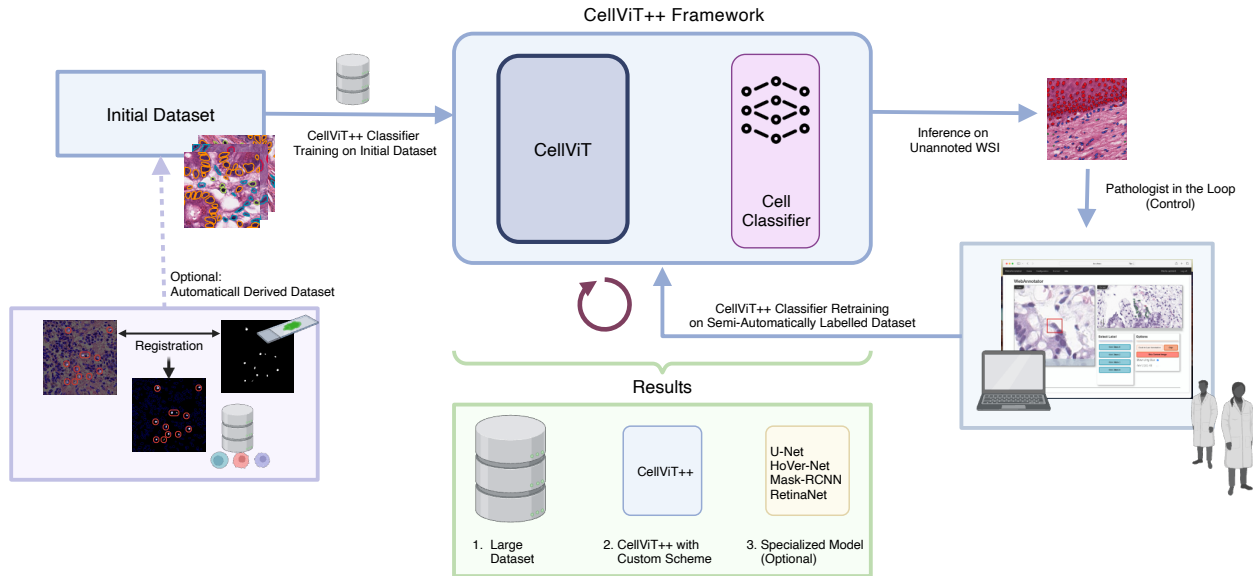


Fig. 5. Suggested workflow for minimal human intervention training.

disease-specific pattern recognition, thereby contributing to personalized treatment strategies and patient stratification. Quantitative analyses of cell shape information are also conceivable.

Despite these advancements, limitations remain. A major concern is the absence of a quality control (QC) module in our current pipeline. As shown by Schömig-Markiefka et al. (2021), segmentation model performance deteriorates significantly when working with suboptimal WSI such as those affected by blurriness or tissue folding. This highlights the importance of incorporating QC during preprocessing to ensure consistent model performance. This is not a model development issue but rather a pipeline optimization task. Additionally, while CellViT⁺⁺ performs well in low-data scenarios, its performance can be surpassed by models specifically trained on large, task-specific datasets, such as Lizard. When sufficient training data is available, our performance saturates, whereas specialized networks have an advantage because their segmentation heads are also fine-tuned. However, the availability of such large datasets remains a significant constraint. For application of the CellViT⁺⁺ framework, we propose the following workflow, as illustrated in Fig. 5: Initially, a cell dataset with limited annotations should either be manually curated or automatically generated. This dataset is then used to finetune CellViT⁺⁺ on the relevant cell classes from the annotated initial training set, establishing a baseline model. As demonstrated in this study, this baseline already is likely to yield strong performance. Building on the trained model, inference is performed on an unlabeled dataset, followed by active labeling in which a pathologist verifies and corrects the model’s predictions (Huang et al., 2024). These semi-automatically generated annotations can be used to create a significantly larger training dataset, which can then serve as input for the training of specialized models, such as Cerberus (Graham et al., 2023) or RetinaNet (Ross & Dollár, 2017). In this workflow, CellViT⁺⁺ operates as a task-agnostic foundation model, enabling the efficient development of task-specific models tailored to particular applications.

To address the problem of data generation and labelling, we have also introduced a workflow (Fig. 1b and 5) for the automatic creation of cell datasets, overcoming a significant bottleneck in this field. This automated dataset generation can perform comparably to manually annotated datasets, representing a major step forward. By utilizing specific antibodies for the target cell type, cell level datasets could be created with minimal expert intervention, significantly reducing the time and resources needed for dataset development. The proposed workflow (Fig. 5) outlines how an automatic training dataset can be created through the careful selection of markers, followed by the generation of a manual validation dataset using a web-based annotation tool. However, it is worth noting that technical expertise is required for image registration, and the selection of IF/IHC stainings still necessitates domain expertise. Only nucleus-staining markers are suitable for this workflow, and further analyses are needed to determine which stains are most appropriate for which cell type.

A further limitation of our approach is its reliance on high-resolution WSI with a spatial resolution of 0.25 $\mu\text{m}/\text{px}$, which may not be available in all laboratories. Although lower-resolution WSIs can be artificially upscaled to 0.25 $\mu\text{m}/\text{px}$, as demonstrated in our experiments on the Lizard dataset, this upscaling may introduce artifacts that affect model performance. Whereas the model’s token size of 16×16 px (HIPT₂₅₆, UNI, SAM-H) or 14×14 px (Virchow, Virchow₂) is generally well-suited for capturing most cellular structures, in edge cases where adjacent cells are smaller than the token size, there may be challenges in distinguishing between cells from different classes that are represented by the same token. Another limitation is the reduced effectiveness of CellViT⁺⁺ when handling rare cell types, such as mitotic figures, which represent only 0.16% of all cells in the MIDOG⁺⁺ dataset. In such cases, the classification module must achieve a high level of accuracy, as errors in identifying these rare cell types can disproportionately influence overall performance.

Future research will focus on improving CellViT⁺⁺ inference time for real-time diagnostic applications, where

speed and efficiency are crucial. While the inference time of CellViT⁺⁺ has already been reduced by 40.39% compared to the original CellViT publication (Hörst et al., 2024a), gigapixel WSIs still require 10-15 minutes for processing, which may be a limitation in clinical environments.

While these limitations need further investigation, the broader implications of our work are significant. Unlike many medical AI studies, which often focus solely on task-specific evaluation and methods, we aim to facilitate widespread adoption by releasing all training code, algorithms, models and derived datasets. This ensures transparency and reproducibility while enabling other researchers to build upon our framework. Additionally, we have developed a web-based viewer and annotation tools (see Fig. 5 and Extended Data Fig. 2) that eliminate the need for local software installation, allowing for seamless integration into clinical environments. By leveraging cloud computing, our approach is designed to be scalable and accessible.

In conclusion, CellViT⁺⁺ marks a significant advancement in digital pathology, providing a robust, adaptable, and efficient framework for high-throughput cell segmentation and classification. By leveraging foundation models and automated dataset generation, CellViT⁺⁺ accelerates research and enhances diagnostic precision. This work underscores the potential of AI, particularly deep learning, in improving diagnostic workflows and, ultimately, patient outcomes. With CellViT⁺⁺, we give researchers and pathologists a tool that streamlines the analysis of complex tissue samples, reducing manual labor and minimizing errors in cell detection. Integrating such models into clinical practice holds the promise of not only enhancing diagnostic accuracy but also offering deeper insights into tumor biology, thereby enabling more data-driven and evidence-based therapeutic decision-making.

CRedit authorship contribution statement

Fabian Hörst: Conceptualization, Methodology, Software, Formal Analysis, Investigation, Data Curation, Writing - Original Draft, Writing - Review & Editing, Visualization. **Moritz Rempe:** Methodology, Writing - Original Draft, Writing - Review & Editing. **Helmut Becker:** Methodology, Writing - Original Draft, Writing - Review & Editing. **Lukas Heine:** Software, Methodology, Writing - Original Draft, Writing - Review & Editing. **Julius Keyl:** Validation, Writing - Review & Editing. **Jens Kleesiek:** Resources, Writing - Review & Editing, Supervision, Project administration, Funding acquisition.

Acknowledgments This work received funding from 'KITE' (Plattform für KI-Translation Essen) from the REACT-EU initiative (<https://kite.ikim.nrw/>, EFRE-0801977) and the Cancer Research Center Cologne Essen (CCCE). The work of Helmut Becker was funded by a PhD grant from the DFG Research Training Group 2535 "Knowledge-and data-based personalization of medicine at the point of care (WisPerMed)". Moritz Rempe and Jens Kleesiek received funding from the Bruno & Helene Jöster Foundation. We acknowledge support by the Open Access Publication Fund of the University of Duisburg-Essen. The authors acknowledge that this manuscript was edited with the assistance of LLMs. The authors declare no competing interests.

The following Figures have been created with BioRender:

- Figure 1: Created in BioRender. Hörst, F. (2025) <https://BioRender.com/j63e764>
- Figure 5: Created in BioRender. Hörst, F. (2025) <https://BioRender.com/u10j553>

- Extended Data Fig. 1: Created in BioRender. Hörst, F. (2025) <https://BioRender.com/v55z265>

References

- Ali, M. (2020). *PyCaret: An open source, low-code machine learning library in Python*. PyCaret version 1.0.0.
- Amgad, M., Atteya, L. A., Hussein, H., Mohammed, K. H., Hafiz, E., Elsebaie, M. A. T., et al. (2022). Nucls: A scalable crowdsourcing approach and dataset for nucleus classification and segmentation in breast cancer. *GigaScience*, 11. DOI: [10.1093/gigascience/giac037](https://doi.org/10.1093/gigascience/giac037).
- Amgad, M., Stovgaard, E. S., Balslev, E., Thagaard, J., Chen, W., Dudgeon, S., et al. (2020). Report on computational assessment of tumor infiltrating lymphocytes from the international immunoncology biomarker working group. *npj Breast Cancer*, 6(1). DOI: [10.1038/s41523-020-0154-2](https://doi.org/10.1038/s41523-020-0154-2).
- Aubreville, M., Wilm, F., Stathonikos, N., Breininger, K., Donovan, T., Jabari, S., et al. (2023). Midog++: A comprehensive multi-domain dataset for mitotic figure detection. DOI: [10.6084/M9.FIGSHARE.C.6615571.V1](https://doi.org/10.6084/M9.FIGSHARE.C.6615571.V1).
- Baidoshvili, A., Bucur, A., van Leeuwen, J., van der Laak, J., Kluijn, P., & van Diest, P. J. (2018). Evaluating the benefits of digital pathology implementation: time savings in laboratory logistics. *Histopathology*, 73(5), 784–794. DOI: [10.1111/his.13691](https://doi.org/10.1111/his.13691).
- Bradski, G. (2000). The OpenCV Library. *Dr. Dobb's Journal of Software Tools*.
- Buslaev, A., Parinov, A., Khvedchenya, E., Iglovikov, V. I., & Kalinin, A. A. K. (2018). AlbuMentations: fast and flexible image augmentations. *arXiv preprint*. DOI: [10.48550/arXiv.1809.06839](https://doi.org/10.48550/arXiv.1809.06839).
- Caron, M., Touvron, H., Misra, I., Jégou, H., Mairal, J., Bojanowski, P., et al. (2021). Emerging properties in self-supervised vision transformers. In *Proceedings of the IEEE/CVF international conference on computer vision* (pp. 9650–9660). DOI: [10.1109/iccv48922.2021.00951](https://doi.org/10.1109/iccv48922.2021.00951).
- Chen, R. J., Chen, C., Li, Y., Chen, T. Y., Trister, A. D., Krishnan, R. G., et al. (2022). Scaling vision transformers to gigapixel images via hierarchical self-supervised learning. In *Proceedings of the IEEE/CVF Conference on Computer Vision and Pattern Recognition* (pp. 16144–16155). DOI: [10.1109/cvpr52688.2022.01567](https://doi.org/10.1109/cvpr52688.2022.01567).
- Chen, R. J., Ding, T., Lu, M. Y., Williamson, D. F. K., Jaume, G., Song, A. H., et al. (2024). Towards a general-purpose foundation model for computational pathology. *Nature Medicine*, 30(3), 850–862. DOI: [10.1038/s41591-024-02857-3](https://doi.org/10.1038/s41591-024-02857-3).
- Chen, T. & Guestrin, C. (2016). Xgboost: A scalable tree boosting system. In *Proceedings of the 22nd acm sigkdd international conference on knowledge discovery and data mining* (pp. 785–794). DOI: [10.1145/2939672.2939785](https://doi.org/10.1145/2939672.2939785).
- Cheng, B., Misra, I., Schwing, A. G., Kirillov, A., & Girdhar, R. (2022). Masked-attention mask transformer for universal image segmentation. In *Proceedings of the IEEE/CVF conference on computer vision and pattern recognition* (pp. 1290–1299). DOI: [10.1109/cvpr52688.2022.00135](https://doi.org/10.1109/cvpr52688.2022.00135).
- Detlefsen, N., Borovec, J., Schock, J., Jha, A., Koker, T., Di Liello, L., et al. (2022). Torchmetrics - measuring reproducibility in pytorch. *Journal of Open Source Software*, 7(70), 4101. DOI: [10.21105/joss.04101](https://doi.org/10.21105/joss.04101).
- Dippel, J., Feulner, B., Winterhoff, T., Schallenberg, S., Dernbach, G., Kunft, A., et al. (2024). Rudolfv: a foundation model by pathologists for pathologists. DOI: [10.48550/ARXIV.2401.04079](https://doi.org/10.48550/ARXIV.2401.04079).
- Dorogush, A. V., Ershov, V., & Gulin, A. (2018). Catboost: gradient boosting with categorical features support. *arXiv preprint*. DOI: [10.48550/arXiv.1810.11363](https://doi.org/10.48550/arXiv.1810.11363).

- Dosovitskiy, A. (2020). An image is worth 16x16 words: Transformers for image recognition at scale. *arXiv preprint*. DOI: [10.48550/arXiv.2010.11929](https://doi.org/10.48550/arXiv.2010.11929).
- Fraggetta, F., L'Imperio, V., Ameisen, D., Carvalho, R., Leh, S., Kiehl, T.-R., et al. (2021). Best practice recommendations for the implementation of a digital pathology workflow in the anatomic pathology laboratory by the european society of digital and integrative pathology (esdip). *Diagnostics*, 11(11), 2167. DOI: [10.3390/diagnostics11112167](https://doi.org/10.3390/diagnostics11112167).
- Gamper, J., Koohbanani, N. A., Benes, K., Graham, S., Jahanifar, M., Khurram, S. A., et al. (2020). Pannuke dataset extension, insights and baselines. *arXiv preprint*. DOI: [10.48550/arXiv.2003.10778](https://doi.org/10.48550/arXiv.2003.10778).
- Goode, A., Gilbert, B., Harkes, J., Jukic, D., & Satyanarayanan, M. (2013). Openslide: A vendor-neutral software foundation for digital pathology. *Journal of pathology informatics*, 4(1), 27. DOI: [10.4103/2153-3539.119005](https://doi.org/10.4103/2153-3539.119005).
- Graham, S., Chen, H., Gamper, J., Dou, Q., Heng, P.-A., Snead, D., et al. (2019a). Mild-net: Minimal information loss dilated network for gland instance segmentation in colon histology images. *Medical Image Analysis*, 52, 199–211. DOI: [10.1016/j.media.2018.12.001](https://doi.org/10.1016/j.media.2018.12.001).
- Graham, S., Jahanifar, M., Azam, A., Nimir, M., Tsang, Y.-W., Dodd, K., et al. (2021). Lizard: A large-scale dataset for colonic nuclear instance segmentation and classification. In *Proceedings of the IEEE/CVF international conference on computer vision* (pp. 684–693). DOI: [10.1109/iccvw54120.2021.00082](https://doi.org/10.1109/iccvw54120.2021.00082).
- Graham, S., Vu, Q. D., Jahanifar, M., Raza, S. E. A., Minhas, F., Snead, D., et al. (2023). One model is all you need: Multi-task learning enables simultaneous histology image segmentation and classification. *Medical Image Analysis*, 83, 102685. DOI: [10.1016/j.media.2022.102685](https://doi.org/10.1016/j.media.2022.102685).
- Graham, S., Vu, Q. D., Raza, S. E. A., Azam, A., Tsang, Y. W., Kwak, J. T., et al. (2019b). Hover-net: Simultaneous segmentation and classification of nuclei in multi-tissue histology images. *Medical Image Analysis*, 58, 101563. DOI: [10.1016/j.media.2019.101563](https://doi.org/10.1016/j.media.2019.101563).
- Grossman, R. L., Heath, A. P., Ferretti, V., Varmus, H. E., Lowy, D. R., Kibbe, W. A., et al. (2016). Toward a shared vision for cancer genomic data. *New England Journal of Medicine*, 375(12), 1109–1112. DOI: <http://dx.doi.org/10.1056/NEJMp1607591>.
- Guo, J., Lu, S., Cui, C., Deng, R., Yao, T., Tao, Z., et al. (2024). Assessment of cell nuclei ai foundation models in kidney pathology. *arXiv preprint*. DOI: [10.48550/arXiv.2408.06381](https://doi.org/10.48550/arXiv.2408.06381).
- Harris, C. R., Millman, K. J., van der Walt, S. J., Gommers, R., Virtanen, P., Cournapeau, D., et al. (2020). Array programming with NumPy. *Nature*, 585(7825), 357–362. DOI: [10.1038/s41586-020-2649-2](https://doi.org/10.1038/s41586-020-2649-2).
- Hatamizadeh, A., Tang, Y., Nath, V., Yang, D., Myronenko, A., Landman, B., et al. (2022). Unetr: Transformers for 3d medical image segmentation. In *Proceedings of the IEEE/CVF winter conference on applications of computer vision* (pp. 574–584). DOI: [10.1109/wacv51458.2022.00181](https://doi.org/10.1109/wacv51458.2022.00181).
- Hörst, F., Rempe, M., Heine, L., Seibold, C., Keyl, J., Kleesiek, J., et al. (2024a). Cellvit: Vision transformers for precise cell segmentation and classification. *Medical Image Analysis*, 94, 103143. DOI: [10.1016/j.media.2024.103143](https://doi.org/10.1016/j.media.2024.103143).
- Hörst, F., Schaheer, S. H., Baldini, G., Bahnsen, F. H., Egger, J., & Kleesiek, J. (2024b). *Accelerating Artificial Intelligence-based Whole Slide Image Analysis with an Optimized Preprocessing Pipeline*, (pp. 356–361). Springer Fachmedien Wiesbaden. DOI: [10.1007/978-3-658-44037-4_91](https://doi.org/10.1007/978-3-658-44037-4_91).
- Huang, Z., Yang, E., Shen, J., Gratzinger, D., Eyerer, F., Liang, B., et al. (2024). A pathologist-AI collaboration framework for enhancing diagnostic accuracies and efficiencies. *Nat. Biomed. Eng.* DOI: [10.1038/s41551-024-01223-5](https://doi.org/10.1038/s41551-024-01223-5).
- Isensee, F., Jaeger, P. F., Kohl, S. A. A., Petersen, J., & Maier-Hein, K. H. (2020). nnu-net: a self-configuring method for deep learning-based biomedical image segmentation. *Nature Methods*, 18(2), 203–211. DOI: [10.1038/s44222-023-00096-8](https://doi.org/10.1038/s44222-023-00096-8).
- Jaume, G., Doucet, P., Song, A. H., Lu, M. Y., Almagro-Pérez, C., Wagner, S. J., et al. (2024). Hest-1k: A dataset for spatial transcriptomics and histology image analysis. DOI: [10.48550/arXiv.2406.16192](https://doi.org/10.48550/arXiv.2406.16192).
- Kirillov, A., He, K., Girshick, R., Rother, C., & Dollar, P. (2019). Panoptic segmentation. In *Proceedings of the IEEE/CVF Conference on Computer Vision and Pattern Recognition (CVPR)* (pp. 9404–9413). DOI: [10.1109/CVPR.2019.00963](https://doi.org/10.1109/CVPR.2019.00963).
- Kirillov, A., Mintun, E., Ravi, N., Mao, H., Rolland, C., Gustafson, L., et al. (2023). Segment anything. *arXiv preprint*. DOI: [10.48550/arXiv.2304.02643](https://doi.org/10.48550/arXiv.2304.02643).
- Klimeck, L., Heisser, T., Hoffmeister, M., & Brenner, H. (2023). Colorectal cancer: A health and economic problem. *Best Practice & Research Clinical Gastroenterology*, 66, 101839. DOI: [10.1016/j.bpg.2023.101839](https://doi.org/10.1016/j.bpg.2023.101839).
- Komura, D., Onoyama, T., Shinbo, K., Odaka, H., Hayakawa, M., Ochi, M., et al. (2023). Restaining-based annotation for cancer histology segmentation to overcome annotation-related limitations among pathologists. *Patterns*, 4(2), 100688. DOI: [10.1016/j.patter.2023.100688](https://doi.org/10.1016/j.patter.2023.100688).
- Koyuncu, D., Tavolara, T., Gatti, D. M., Gower, A. C., Ginese, M. L., Kramnik, I., et al. (2024). B cells in perivascular and peribronchiolar granuloma-associated lymphoid tissue and b-cell signatures identify asymptomatic mycobacterium tuberculosis lung infection in diversity outbred mice. *Infection and Immunity*, 92(7). DOI: [10.1128/iai.00263-23](https://doi.org/10.1128/iai.00263-23).
- Lacoste, A., Luccioni, A., Schmidt, V., & Dandres, T. (2019). Quantifying the carbon emissions of machine learning. *arXiv preprint*. DOI: [10.48550/arXiv.1910.09700](https://doi.org/10.48550/arXiv.1910.09700).
- Lafarge, M. W. & Koelzer, V. H. (2024). *Detecting Cells in Histopathology Images with a ResNet Ensemble Model*, (pp. 123–129). Springer Nature Switzerland. DOI: [10.1007/978-3-031-55088-1_11](https://doi.org/10.1007/978-3-031-55088-1_11).
- Lam, S. K., Pitrou, A., & Seibert, S. (2015). Numba: a llvm-based python jit compiler. In *Proceedings of the Second Workshop on the LLVM Compiler Infrastructure in HPC*, SC15: ACM. DOI: [10.1145/2833157.2833162](https://doi.org/10.1145/2833157.2833162).
- Lee, H. H., Gu, Y., Zhao, T., Xu, Y., Yang, J., Usuyama, N., et al. (2024). Foundation models for biomedical image segmentation: A survey. *arXiv preprint*. DOI: [10.48550/arXiv.2401.07654](https://doi.org/10.48550/arXiv.2401.07654).
- Li, Z., Li, W., Mai, H., Zhang, T., & Xiong, Z. (2024). *Enhancing Cell Detection in Histopathology Images: A ViT-Based U-Net Approach*, (pp. 150–160). Springer Nature Switzerland. DOI: http://dx.doi.org/10.1007/978-3-031-55088-1_14.
- Liu, S., Amgad, M., More, D., Rathore, M. A., Salgado, R., & Cooper, L. A. D. (2024). A panoptic segmentation dataset and deep-learning approach for explainable scoring of tumor-infiltrating lymphocytes. *npj Breast Cancer*, 10(1). DOI: [10.1038/s41523-024-00663-1](https://doi.org/10.1038/s41523-024-00663-1).
- Lo, Y.-W. & Yang, C.-H. (2024). *Enhancing Cell Detection via FC-HarDNet and Tissue Segmentation: OCELOT 2023 Challenge Approach*, (pp. 130–137). Springer Nature Switzerland. DOI: [10.1007/978-3-031-55088-1_12](https://doi.org/10.1007/978-3-031-55088-1_12).

- Millward, J., He, Z., & Nibali, A. (2024). *Dense Prediction of Cell Centroids Using Tissue Context and Cell Refinement*, (pp. 138–149). Springer Nature Switzerland. DOI: [10.1007/978-3-031-55088-1_13](https://doi.org/10.1007/978-3-031-55088-1_13).
- Moritz, P., Nishihara, R., Wang, S., Tumanov, A., Liaw, R., Liang, E., et al. (2018). Ray: A distributed framework for emerging AI applications. In *13th USENIX symposium on operating systems design and implementation (OSDI 18)* (pp. 561–577).
- Naylor, P., Laé, M., Reyat, F., & Walter, T. (2019). Segmentation of nuclei in histopathology images by deep regression of the distance map. *IEEE Transactions on Medical Imaging*, 38(2), 448–459. DOI: [10.1109/TMI.2018.2865709](https://doi.org/10.1109/TMI.2018.2865709).
- Okuta, R., Unno, Y., Nishino, D., Hido, S., & Loomis, C. (2017). Cupy: A numpy-compatible library for nvidia gpu calculations. In *Proceedings of Workshop on Machine Learning Systems (LearningSys) in The Thirty-first Annual Conference on Neural Information Processing Systems (NIPS)*.
- Oquab, M., Darcet, T., Moutakanni, T., Vo, H., Szafraniec, M., Khalidov, V., et al. (2023). Dinov2: Learning robust visual features without supervision. *arXiv preprint*. DOI: [10.48550/arXiv.2304.07193](https://doi.org/10.48550/arXiv.2304.07193).
- Paszke, A., Gross, S., Massa, F., Lerer, A., Bradbury, J., Chanan, G., et al. (2019). Pytorch: An imperative style, high-performance deep learning library. *arXiv preprint*. DOI: [10.48550/arXiv.1912.01703](https://doi.org/10.48550/arXiv.1912.01703).
- Patterson, D., Gonzalez, J., Le, Q., Liang, C., Munguia, L.-M., Rothchild, D., et al. (2021). Carbon emissions and large neural network training. *arXiv preprint*. DOI: [10.48550/arXiv.2104.10350](https://doi.org/10.48550/arXiv.2104.10350).
- Pedregosa, F., Varoquaux, G., Gramfort, A., Michel, V., Thirion, B., Grisel, O., et al. (2011). Scikit-learn: Machine learning in Python. *Journal of Machine Learning Research*, 12, 2825–2830.
- Pocock, J., Graham, S., Vu, Q. D., Jahanifar, M., Deshpande, S., Hadjigeorgiou, G., et al. (2022). TIAToolbox as an end-to-end library for advanced tissue image analytics. *Communications Medicine*, 2(1), 120. DOI: [10.1038/s43856-022-00186-5](https://doi.org/10.1038/s43856-022-00186-5).
- Raghaw, C. S., Sharma, A., Bansal, S., Rehman, M. Z. U., & Kumar, N. (2024). Cotconet: An optimized coupled transformer-convolutional network with an adaptive graph reconstruction for leukemia detection. *Computers in Biology and Medicine*, 179, 108821. DOI: [10.1016/j.compbiomed.2024.108821](https://doi.org/10.1016/j.compbiomed.2024.108821).
- Ravi, N., Gabeur, V., Hu, Y.-T., Hu, R., Ryali, C., Ma, T., et al. (2024). Sam 2: Segment anything in images and videos. *arXiv preprint*. DOI: [10.48550/arXiv.2408.00714](https://doi.org/10.48550/arXiv.2408.00714).
- Reiss, S., Seibold, C., Freytag, A., Rodner, E., & Stiefelhagen, R. (2021). Every annotation counts: Multi-label deep supervision for medical image segmentation. In *Proceedings of the IEEE/CVF Conference on Computer Vision and Pattern Recognition (CVPR)* (pp. 9532–9542). DOI: [10.1109/cvpr46437.2021.00941](https://doi.org/10.1109/cvpr46437.2021.00941).
- Ross, T.-Y. & Dollár, G. (2017). Focal loss for dense object detection. In *proceedings of the IEEE conference on computer vision and pattern recognition* (pp. 2980–2988).
- Ryu, J., Puche, A. V., Shin, J., Park, S., Brattoli, B., Lee, J., et al. (2023). Ocelot: overlapped cell on tissue dataset for histopathology. In *Proceedings of the IEEE/CVF Conference on Computer Vision and Pattern Recognition* (pp. 23902–23912). DOI: [10.1109/cvpr52729.2023.02289](https://doi.org/10.1109/cvpr52729.2023.02289).
- Salgado, R., Denkert, C., Demaria, S., Sirtaine, N., Klauschen, F., Pruneri, G., et al. (2015). The evaluation of tumor-infiltrating lymphocytes (tils) in breast cancer: recommendations by an international tils working group 2014. *Annals of Oncology*, 26(2), 259–271. DOI: [10.1093/annonc/mdl450](https://doi.org/10.1093/annonc/mdl450).
- Schoenpflug, L. A. & Koelzer, V. H. (2024). *SoftCTM: Cell Detection by Soft Instance Segmentation and Consideration of Cell-Tissue Interaction*, (pp. 109–122). Springer Nature Switzerland. DOI: [10.1007/978-3-031-55088-1_10](https://doi.org/10.1007/978-3-031-55088-1_10).
- Schömig-Markiefka, B., Pryalukhin, A., Hulla, W., Bychkov, A., Fukuoka, J., Madabhushi, A., et al. (2021). Quality control stress test for deep learning-based diagnostic model in digital pathology. *Modern Pathology*, 34(12), 2098–2108. DOI: [10.1038/s41379-021-00859-x](https://doi.org/10.1038/s41379-021-00859-x).
- Shafi, S. & Parwani, A. V. (2023). Artificial intelligence in diagnostic pathology. *Diagnostic Pathology*, 18(1). DOI: [10.1186/s13000-023-01375-z](https://doi.org/10.1186/s13000-023-01375-z).
- Sirinukunwattana, K., Pluim, J. P., Chen, H., Qi, X., Heng, P.-A., Guo, Y. B., et al. (2017). Gland segmentation in colon histology images: The glas challenge contest. *Medical Image Analysis*, 35, 489–502. DOI: [10.1016/j.media.2016.08.008](https://doi.org/10.1016/j.media.2016.08.008).
- Song, A. H., Jaume, G., Williamson, D. F. K., Lu, M. Y., Vaidya, A., Miller, T. R., et al. (2023). Artificial intelligence for digital and computational pathology. *Nature Reviews Bioengineering*, 1(12), 930–949. DOI: [10.1038/s44222-023-00096-8](https://doi.org/10.1038/s44222-023-00096-8).
- Stringer, C., Wang, T., Michaelos, M., & Pachitariu, M. (2021). Cellpose: a generalist algorithm for cellular segmentation. *Nature methods*, 18(1), 100–106. DOI: [10.1101/2020.02.02.931238](https://doi.org/10.1101/2020.02.02.931238).
- Sun, P., He, J., Chao, X., Chen, K., Xu, Y., Huang, Q., et al. (2021). A computational tumor-infiltrating lymphocyte assessment method comparable with visual reporting guidelines for triple-negative breast cancer. *EBioMedicine*, 70, 103492. DOI: [10.1016/j.ebiom.2021.103492](https://doi.org/10.1016/j.ebiom.2021.103492).
- The pandas development team (2024). pandas-dev/pandas: Pandas. DOI: [10.5281/zenodo.3509134](https://doi.org/10.5281/zenodo.3509134).
- Van der Walt, S., Schönberger, J. L., Nunez-Iglesias, J., Boulogne, F., Warner, J. D., Yager, N., et al. (2014). scikit-image: image processing in python. *PeerJ*, 2, e453.
- Virtanen, P., Gommers, R., Oliphant, T. E., Haberland, M., Reddy, T., Cournapeau, D., et al. (2020). SciPy 1.0: Fundamental Algorithms for Scientific Computing in Python. *Nature Methods*, 17, 261–272. DOI: [10.1038/s41592-019-0686-2](https://doi.org/10.1038/s41592-019-0686-2).
- Vorontsov, E., Bozkurt, A., Casson, A., Shaikovski, G., Zelechowski, M., Severson, K., et al. (2024). A foundation model for clinical-grade computational pathology and rare cancers detection. *Nature Medicine*. DOI: [10.1038/s41591-024-03141-0](https://doi.org/10.1038/s41591-024-03141-0).
- Wang, X., Yang, S., Zhang, J., Wang, M., Zhang, J., Yang, W., et al. (2022). Transformer-based unsupervised contrastive learning for histopathological image classification. *Medical Image Analysis*, 81, 102559. DOI: [10.1016/j.media.2022.102559](https://doi.org/10.1016/j.media.2022.102559).
- Waring, J., Lindvall, C., & Umeton, R. (2020). Automated machine learning: Review of the state-of-the-art and opportunities for healthcare. *Artificial Intelligence in Medicine*, 104, 101822. DOI: [10.1016/j.artmed.2020.101822](https://doi.org/10.1016/j.artmed.2020.101822).
- Weigert, M. & Schmidt, U. (2022). Nuclei instance segmentation and classification in histopathology images with stardist. In *2022 IEEE International Symposium on Biomedical Imaging Challenges (ISBIC)* (pp. 1–4).: IEEE. DOI: [10.1109/isbic56247.2022.9854534](https://doi.org/10.1109/isbic56247.2022.9854534).
- Wightman, R. (2019). Pytorch image models. <https://github.com/rwightman/pytorch-image-models>. DOI: [10.5281/zenodo.4414861](https://doi.org/10.5281/zenodo.4414861).
- World Health Organization: Regional Office for Europe (2020). *World cancer report*. IARC.
- Wu, G., Segovis, C. M., Nicola, L. P., & Chen, M. M. (2023). Current reimbursement landscape of artificial intelligence. *Journal of the American College of Radiology*, 20(10), 957–961. DOI: [10.1016/j.jacr.2023.07.018](https://doi.org/10.1016/j.jacr.2023.07.018).

Xu, H., Usuyama, N., Bagga, J., Zhang, S., Rao, R., Naumann, T., et al. (2024). A whole-slide foundation model for digital pathology from real-world data. *Nature*, (pp. 1–8). DOI: [10.1038/s41586-024-07441-w](https://doi.org/10.1038/s41586-024-07441-w).

Yao, K., Huang, K., Sun, J., & Hussain, A. (2023). Pointnu-net: Keypoint-assisted convolutional neural network for simultaneous multi-tissue histology nuclei segmentation and classification. *IEEE Transactions on Emerging Topics in Computational Intelligence*, 8(1), 802–813. DOI: [10.1109/tetci.2023.3281864](https://doi.org/10.1109/tetci.2023.3281864).

Zhong, Y., Li, X., Mei, H., & Xiong, S. (2023). *Probability-Based Nuclei Detection and Critical-Region Guided Instance Segmentation*, (pp. 122–135). Springer Nature Singapore. DOI: [10.1007/978-981-99-8558-6_11](https://doi.org/10.1007/978-981-99-8558-6_11).

Zimmermann, E., Vorontsov, E., Viret, J., Casson, A., Zelechowski, M., Shaikovski, G., et al. (2024). Virchow2: Scaling self-supervised mixed magnification models in pathology. *arXiv preprint*. DOI: [10.48550/arXiv.2408.00738](https://doi.org/10.48550/arXiv.2408.00738).

Methods

Network Architecture

CellViT. CellViT is a deep learning architecture designed specifically for nuclei segmentation and classification in histopathological images. The architecture is inspired by the UNETR (Hatamizadeh et al., 2022) network, adapted for 2D images, resulting in a U-shaped structure consisting of an image encoder and segmentation decoders. To facilitate the task of nuclei segmentation and to allow the network to separate overlapping nuclei, CellViT employs three distinct multi-task decoder branches (Graham et al., 2019b). The first branch predicts the binary segmentation map of all nuclei, the second generates horizontal and vertical distance maps to provide spatial information to delineate the nuclei and the third branch predicts the nuclei type map, enabling the classification into the PanNuke nuclei classes (Hörst et al., 2024a), which we removed in this study. To integrate the outputs from these branches, we use the postprocessing strategy of HoVer-Net to split up overlapping nuclei. The core of CellViT leverages the Vision Transformer architecture to encode images, which is an adaptation of the Transformer model originally developed for natural language processing tailored for image analysis. Given an input image $x \in \mathbb{R}^{H \times W \times 3}$ with height H , width W and 3 input channels, the image is divided into a sequence of flattened tokens $x_p \in \mathbb{R}^{N \times (P^2 \cdot 3)}$, $N = HW/P^2$. Each of these tokens is a squared image section with the dimension $P \times P$, mapped by a linear projection layer into a D dimensional latent space vector $z_0 \in \mathbb{R}^D$ whose size remains constant through all of the Transformer layers $l = 1 \dots L$, resulting in a token matrix $z_0 \in \mathbb{R}^{(N+k) \times D}$. Additional tokens such like the class token [CLS] or register tokens [REG] are summarized in the scalar k . Each of the Transformer layers l consists of the self-attention mechanism with H heads, updating the tokens $z_l = f(z_{l-1})$, $l = 1 \dots L$, successively. Using this approach, ViTs are able to capture complex spatial relationships across the image as each token attends to all remaining tokens. Additionally, five skip connections are added between the ViT encoder at different depth levels l and the corresponding upsampling path for information passing to the upsampling decoder branches.

Using this method, we achieved outstanding results on the PanNuke dataset and demonstrated the generalizability of our model to new datasets with significant distributional differences. This underscores the robustness and adaptability of our approach to distribution shifts. The most important factor contributing to this performance improvement was that the ViT encoder architecture allowed us to use large pretrained networks, so-called foundation models.

Inference. Although all CellViT models were initially trained using input images of 256×256 px, WSI-wise inference is performed on image sections of $1,024 \times 1,024$ px size with an overlap of 64 px. To accelerate postprocessing, we optimized the HoVer-Net postprocessing strategy to run on CUDA-enabled GPUs by utilizing libraries such as Numba (Lam et al., 2015), CuPY (Okuta et al., 2017) and Ray (Moritz et al., 2018). This optimization enables efficient, independent parallel processing of each patch within a batch on GPUs.

The final step involves merging overlapping cells, a process that incurs minimal computational overhead due to the relatively small number of overlapping cells compared to the total number of cells in a WSI. By optimizing the pipeline, we achieved a 40.38% reduction in runtime (SD 4.77%) on a test dataset consisting of 10 diverse WSIs, compared to our original publication of CellViT (Hörst et al., 2024a).

Token based Cell Classification Module and CellViT⁺⁺. As outlined in the introduction to the CellViT model, our approach primarily relies on a ViT-based image encoder, where the input data is represented and processed as tokens $z_l \in \mathbb{R}^{(N+k) \times D}$ at each layer l . Given that WSI adhere to a fixed physical optical scale - defined by a consistent magnification through a microscope, typically with a resolution of $0.25 \mu\text{m}/\text{px}$ at $\times 40$ magnification or $0.50 \mu\text{m}/\text{px}$ at $\times 20$ magnification - a consistent mapping between the objects within the image and the corresponding tokens can be established, which remains constant across WSIs with identical scanning setups. Given an input resolution of $0.25 \mu\text{m}/\text{px}$ of the images for the CellViT segmentation algorithm and a token size of $P = 14$ px or $P = 16$ px, each token corresponds to approximately $4 \mu\text{m}$, which is in the range of the size of a human cell nuclei (Chen et al., 2022). Excluding the [CLS] token and any potential register tokens [Reg], the token matrices z_l of the respective Transformer layers l can be rearranged into a three-dimensional tensor $Z_j \in \mathbb{R}^{\frac{H}{P} \times \frac{W}{P} \times D}$, where the first two dimensions correspond to the spatial arrangement analogous to the input WSI sections. This spatial arrangement, coupled with the fact that the size of each token roughly matches that of a nucleus, allows for the assignment of tokens $z_l^{\hat{y}_j} \in \mathbb{R}^D$ to each detected cell \hat{y}_j . Since each layer l further abstracts and enriches the tokens with additional information, we only assign each cell the token $z_L^{\hat{y}_j}$ of the output of the last Transformer L , thereby generating an embedding vector for each cell. Consequently, in the CellViT model, tokens from the last Transformer layer of the ViT encoder can be directly mapped to individual cells detected at the output of the segmentation head. This structure allows for efficient computation of deep cell features directly within the forward pass of the model. If a nucleus is associated with multiple tokens, we average over all token embeddings in which the nucleus is located.

A significant advantage of our method is that the cell embedding vectors can be directly extracted during a forward pass of or CellViT segmentation models. In contrast, existing two-stage models consists of a segmentation model and a separate feature extraction method. For this, visual crops of the segmented cells serves as inputs for a second model that either extract classical image features, like by Huang et al. (2024), or computes an embedding vector using another deep learning model. This two-stage approach introduces considerable overhead regarding computational time and memory, as the number of cells in a typical WSI can range from several hundred thousand to millions. By extracting cell embeddings jointly with the segmentation process, our method eliminates this overhead, as the tokens are inherently present within the ViT encoder.

In this work, cell tokens are utilized to extend the CellViT model to include new cell classes. We achieve this by extracting cell embeddings from annotated datasets, where each cell is assigned a class label. This process results in a dataset comprising cell embedding vectors paired with their corresponding cell labels. We then train a classifier to predict the cell class based on these tokens. This information can be leveraged in the post-processing stage to adaptively adjust the cell classes that CellViT can recognize, which are initially limited to the PanNuke classes. Each cell at the output is then assigned the prediction of our cell classification module. This approach allows for the inclusion of more fine-grained cell categories or the definition of organ-specific classes. We denote this combination of segmentation models and the lightweight cell classification module as CellViT⁺⁺.

For the classifier, we employ a fully connected feedforward network with one hidden layer and a ReLU activation function. To avoid negatively impacting downstream segmentation performance and for efficiency reasons, only the classifier is re-trained based on the tokens and cell labels, while the CellViT⁺⁺ segmentation network remains unchanged.

Foundation Models

As previously mentioned, the primary motivation behind the development of the CellViT architecture was to create a network structure capable of leveraging domain-specific and task-specific foundation models for fine-grained cell segmentation and detection, based on the ViT architecture. A list of the included foundation models and their specifications is provided in this section, with the networks organized in ascending order based on the number of parameters. The models HIPT₂₅₆, UNI, Virchow and Virchow₂ are all histopathological foundation models, while SAM is a task specific foundation model for image segmentation.

HIPT₂₅₆. In 2022 [Chen et al. \(2022\)](#) introduced one of the first foundation models for histopathological slide analysis, called Hierarchical Image Pyramid Transformer (HIPT). The HIPT model is a hierarchical network designed for slide-level representation extraction by stacking multiple ViT-stages on top of each other. The architecture employs a three-stage hierarchical structure performing aggregation from cell-level over micro-tissue structure up to whole slide representation. In total, their network consists of three stages, with each stage independently pretrained using DINO ([Caron et al., 2021](#)). The HIPT₂₅₆ model refers specifically to the first stage, which processes 16×16 px-sized visual tokens extracted from 256×256 px patches to create a local cell-cluster token ([Hörst et al., 2024a](#)), employing a vanilla ViT-Small (ViT-S) architecture with 21.7 million parameters. The stage was pretrained on 104 million patches extracted from 10,678 slides of TCGA. By analyzing the attention heatmaps of the Transformer layers within the ViT, [Chen et al. \(2022\)](#) showed that the network effectively learned visual concepts specific to histopathological images, including cell-locations. This makes HIPT₂₅₆ a powerful pretrained backbone for our CellViT⁺⁺ model. Notably, it is the smallest encoder we have examined in this study, with only 3.3 % parameter count of our largest model with ViT-H backbone. The ViT-S specifications are $P = 16, D = 384, L = 12, H = 6$.

UNI. UNI, developed by the same group as HIPT₂₅₆, was specifically tailored to be a general-purpose model for computational pathology to generate patch embeddings. To increase the versatility of UNI, the authors used a more diverse dataset for pretraining, utilizing an internal dataset of more than 100,000 diagnostic WSIs across 20 major tissue types ([Chen et al., 2024](#)). This dataset is one of the largest available collections of WSI and one magnitude larger than the commonly used TCGA dataset. The model was pretrained using DinoV2 ([Oquab et al., 2023](#)) self-supervised training algorithm with more than 100 million patches and is based on a ViT-L architecture with 307 million parameters. UNI excels in weakly supervised slide-level classification tasks, outperforming competitive pretrained encoders. However, as [Chen et al. \(2024\)](#) note, UNI lacks vision-specific biases for solving dense prediction tasks even though they showed competitive segmentation results using Mask2Former approach ([Cheng et al., 2022](#)), but without the capability to perform instance-wise segmentation. The ViT-L backbone has the following specification: $P = 16, D = 1024, L = 24, H = 12$.

Virchow. The Virchow ([Vorontsov et al., 2024](#)) model represents an advancement over UNI with slightly better performance in a cancer detection comparison, outperforming UNI on 13 out of 16 cancer types. Similarly to UNI, the model was trained with DinoV2 ([Oquab et al., 2023](#)) on an internal dataset comprising 1,488,550 WSIs from 119,629 patients. For this, 2 billion tiles were randomly sampled from these WSIs. The architecture employs a ViT-H model with 632 million parameters, but differing from all the previous networks, with a token size of 14×14 px. Thus, to align all models, we reshaped the PanNuke training patches from 256×256 px to 252×252 px and performed inference on rescaled $1,022 \times 1,022$ px instead of $1,024 \times 1,024$ px patches. The model's parameters include an embedding dimension of $D = 1280, L = 32$ Transformer layers, and $H = 16$ attention heads.

Virchow₂. Virchow₂ builds upon the Virchow model by incorporating additional register tokens into the ViT structure and further training on an expanded dataset of 3.1 million histopathology WSIs, derived from 225,401 patients across multiple magnifications ($\times 5, \times 10, \times 20$, and $\times 40$) and staining techniques (H&E and IHC) ([Zimmermann et al., 2024](#)). This dataset extends the original Virchow

dataset and includes nearly 200 tissue types, with 15% of the WSIs and 57% of the patients sourced from diverse institutions worldwide. Trained with an adapted DINOv2 self-supervised learning algorithm, Virchow₂ outperforms both UNI and Virchow on average across eight public tile-level classification benchmarks such as CRC-100k (colorectal cancer morphology classification), Camelyon16 (lymph node metastasis detection in breast cancer) or the challenging Hest-1k dataset (spatial transcriptomics) ([Jaume et al., 2024](#)), demonstrating its robustness across a wide range of applications. On average, Virchow₂ achieved an F_1 -score of 0.885, Virchow of 0.877, and UNI of 0.866. The model's parameters remain consistent with those of Virchow (ViT-H) but with the addition of 4 register tokens ($P = 14, D = 1280, L = 32, H = 16$).

Segment Anything. In the field of natural image processing, [Kirillov et al. \(2023\)](#) introduced the Segment Anything Model (SAM), an open-source segmentation model designed for semantic segmentation. SAM's architecture consists of an image encoder based on the ViT model and a lightweight mask decoder network. The model is available in three different sizes - SAM-B, SAM-L, and SAM-H - corresponding to ViT-Base, ViT-Large, and ViT-Huge architectures, respectively. The final backbone, SAM-H, was trained in a supervised manner on 1.1 billion segmentation masks from 11 million images. According to our previous study ([Hörst et al., 2024a](#)), CellViT with SAM-H backbone outperforms its smaller counterparts in cell segmentation, making it the preferred backbone for this task, with 632 million parameters. Recently, the model was updated with a memory module to capture temporal consistencies in videos, termed SAM-2 ([Ravi et al., 2024](#)). However, for applications not involving time series image data, the original SAM model performs equivalently. This work is limited to the ViT-H backbone (SAM-H), with $P = 16, D = 1280, L = 32$, and $H = 16$. [Abstract von Lee et al. \(2024\)](#) Recent advancements in biomedical image analysis have been significantly driven by the Segment Anything Model (SAM). This transformative technology, originally developed for general-purpose computer vision, has found rapid application in medical image processing. Within the last year, marked by over 100 publications, SAM has demonstrated its prowess in zero-shot learning adaptations for medical imaging. The fundamental promise of SAM lies in its capability to segment or identify objects in images without prior knowledge of the object type or imaging modality.

Experimental Setup

The primary aim of this study is to assess how effectively cell embeddings generated by CellViT⁺⁺ in a single forward pass can be leveraged to train classifiers for newly defined cell classes. Additionally, the study explores variations in cell embeddings across different foundation models and evaluates their efficacy for cell classification tasks. To this end, we employed a variety of datasets, including two multi-organ datasets (Ocelot and MIDOG++) featuring organs not present in the PanNuke training dataset. Furthermore, we assessed CellViT⁺⁺ on two prevalent cancer types: breast cancer, the most commonly diagnosed cancer in women (2.1 million new cases in 2018), using the NuCLS, SegPath, and PanopTILs datasets, and colorectal cancer, the third most common cancer overall (1.8 million new cases in 2018), using the CoNSEP and Lizard datasets.

Despite differences in scope, cell types, and dataset composition, all datasets follow a consistent structure. Each consists of a training set and an externally defined test set, with original publication splits adhered to for comparability. Some datasets, such as Ocelot, include validation splits, while others, like Lizard, use a cross-validation strategy (3-fold in this case). For datasets lacking explicit validation data definitions, we conducted 5-fold CV within the training data and applied models from each fold to the external test dataset. For datasets with validation splits but without CV strategies, experiments were performed using five different random seeds, resulting in five models. Reported results represent the mean scores across these models (except Lizard, which uses 3-fold CV). Any deviations from this methodology are specified in the respective experimental sections.

For each experiment and CellViT-variant, hyperparameter tuning was initially performed with 100 random runs on the training-validation split or the first CV fold, optimizing the classifier's hyperparameters based on validation performance. The tuned hyperparameters included the hidden dimension of the classifier, the

learning rate, and the weight decay of the optimizer. Additionally, we examined the impact of exponential learning rate scheduling with a factor of $\gamma = 0.95$ versus a constant learning rate reduced by half after half the training epochs. This tuning was conducted without data augmentation to minimize runtime. Due to the lack of data augmentation, training and validation cells could be cached after the initial epoch, allowing hyperparameter tuning to be completed within a few hours.

Training setup We used the AdamW optimizer with weight decay and $\beta_1 = 0.85$ and $\beta_2 = 0.9$. Training was conducted with a batch size of 256 over 50 epochs, applying early stopping after 10 epochs without improvement of the area under receiver operating characteristics curve of the classifier. Additionally, we used dropout with a rate of 0.1 as regularization technique. As the CellViT model was trained with mixed precision (AMP training), we also train the classification module with mixed precision. Data caching of CellViT++ cell detections along with the tokens was enabled after the first epoch when no data augmentation was used, which is the default configuration. Images were normalized according to the normalization parameters of the foundation models. All experiments were conducted on a NVIDIA A100 GPU with 80 GB VRAM on a workstation equipped with 24 CPUs and 76GB RAM. However, most of the computations here could be reasonably performed on smaller GPUs (e.g., NVIDIA RTX A5000 with 24 GB VRAM) as well.

Classical Nuclei Feature Calculation

To evaluate the effectiveness of embeddings generated by CellViT++, we compared them against traditional two-stage models, where CellViT++ was employed specifically for cell segmentation which are subsequently used to extract classical features accordingly to Huang et al. (2024). The feature set used in this comparison consists of 128 distinct features, encompassing the 122 classical features of Nuclei.io (Huang et al., 2024). We introduced six additional features related to cytoplasmic region and texture analysis. A list of all features can be found in the publication of Huang et al. (2024). These features capture a range of color, morphological, textural, and spatial properties of the nuclei and cytoplasm. The cytoplasmic region was defined as a 40-by-40 pixel area centered on the nucleus at a resolution of 0.25 $\mu\text{m}/\text{px}$, allowing for a consistent analysis across samples.

For the development of cell classifiers using classical cell features, we compared the three-layer fully connected classification module we use with the CellViT++ token approach with traditional machine learning algorithms, including logistic regression, decision trees, XGBoost, and CatBoost (see Supplementary Table S19). We incorporated the auto-ML tool PyCaret into our pipeline for systematic evaluation and selection of the optimal classification method based on the training data. Through this process, CatBoost demonstrated superior performance across multiple metrics, thereby establishing it as the most effective classical algorithm for our experiments. Consequently, we limited our analysis to CatBoost as a representative classical machine learning technique in our study.

Datasets

Ocelot. The Ocelot dataset (Ryu et al., 2023) is a tumor cell detection dataset to advance the understanding of cell-tissue interaction across multiple human organ systems. It contains a total of 113,026 cells, annotated to differentiate between tumor and non-tumor cells. These cells were derived from human specimens from the TCGA dataset of six organs: Bladder, endometrium, head/neck, kidney, prostate, and stomach. In total, the datasets consists of 664 patches extracted from 303 WSI, with each patch measuring $1,024 \times 1,024$ px. Each patch was acquired at 0.20 $\mu\text{m}/\text{px}$ at a magnification of $\times 40$. While the original dataset also includes region-level fields of view for each cell-level patch to assess whether context regions can improve tumor cell detection, this study focuses exclusively on the annotated cell-level dataset. The dataset is divided into three subsets, training (400 patches), validation (137 patches), and test (126 patches), with a 6:2:2 split ratio at WSI level to prevent leakage (Ryu et al., 2023). The tumor cell distribution is consistent among all three subsets, with around 65% tumor cells and 35% non-tumor cells. In addition to the full training dataset, we further splitted the dataset

into smaller training subsets to assess model performance under limited data conditions. These subsets consist of 5% (18 patches), 10% (44 patches), 25% (103 patches), 50% (201 patches) and 75% (300 patches) of the total training data, allowing for an analysis in regard of data efficiency. A table with detailed information about the split and the cell amount is given in the Supplement (Tab. S3). Annotations were performed by board-certified pathologists with a census strategy among three independent pathologists for each patch. The dataset does not provide segmentation masks of cell contours.

For a fair comparison, all baseline experiments using the Soft-CTM model have been conducted on the Ocelot dataset including the region-wise tumor segmentation masks.

MIDOG++. The MIDOG++ dataset is an extended version of the original MIDOG challenge dataset, designed for mitotic figure detection in histopathology images (Aubreville et al., 2023). It represents the most extensive multi-domain mitotic figure dataset to date, incorporating images from multiple centers, including UMC Utrecht, VMU Vienna, FU Berlin, and AMC New York. The dataset was acquired using multiple scanners to evaluate domain generalization, with images captured at a resolution of 0.23 to 0.25 $\mu\text{m}/\text{px}$, comprising a total of 503 images. The dataset includes 111 test images, representing a 20% stratified split. For each experiment, we performed a stratified 5-fold cross-validation, as suggested by the authors. Annotations in MIDOG++ were generated through a multi-expert consensus strategy, involving expert-level reviews and validation by an automated algorithm. The dataset contains a total of 11,937 annotated mitotic figures and 14,351 hard negatives. Utilizing the CellViT++_{SAM-H} model, we extracted a total of 7,398,795 cells, with mitotic figures representing only 0.16% of all cells. The image tiles have varying sizes, with an average width of 6,804 pixels and an average height of 5,102 pixels, covering larger sections than any other comparable datasets in this study. The primary evaluation metric for this dataset is the F_1 -score. We compared CellViT++ with the object detection model RetinaNet, trained by Aubreville et al. (2023).

CoNSEP (Colorectal Nuclear Segmentation and Phenotypes). This dataset was introduced as part of the HoVer-Net publication (Graham et al., 2019b) and comprises 41 image tiles derived from colon cancer patients at the University Hospitals Coventry and Warwickshire, UK. Each tile measures $num1000 \times num1000$ px, with a resolution of 0.25 $\mu\text{m}/\text{px}$ ($\times 40$). The dataset includes various cell types such as inflammatory cells, healthy epithelial cells, dysplastic/malignant epithelial cells, fibroblasts, muscle cells, and endothelial cells. The annotations were initially performed by one pathologist for each slide, with a second pathologist reviewing the annotations to reach a consensus. Aligned with HoVer-Net, we group normal and dysplastic/malignant epithelial cells under a single epithelial category, and fibroblasts, muscle cells, and endothelial cells under a spindle-shaped nuclei category. The dataset is divided into 27 training tiles and 14 test tiles. To facilitate algorithmic comparisons, we conducted 5-fold CV on the training images, with the final evaluation carried out on the test images. Additionally, we mimicked an iterative labeling approach to assess the cell classification module performance with limited training data. Starting with a single annotated tile, we incrementally increased the number of annotated tiles up to 15, evaluating the impact on model performance at each step. A detailed overview of the number of tiles used at each stage is provided in Supplementary Table S6. The dataset provides segmentation masks such that in addition to the detection capability, also the segmentation performance can be evaluated.

Lizard. The Lizard dataset (Graham et al., 2021) extends the CoNSEP dataset by integrating colon cancer tissue from multiple sources, including PanNuke (Gamper et al., 2020), Glas (Sirinukunwattana et al., 2017), CRAG (Graham et al., 2019a), DigestPath, TCGA (Grossman et al., 2016), and CoNSEP (Graham et al., 2019b). The dataset includes contributions from University Hospitals Coventry and Warwickshire, UK, multiple centers in the USA, and four hospitals in China (Graham et al., 2021). Unlike other datasets used in this study, the Lizard dataset was acquired at a resolution of 0.50 $\mu\text{m}/\text{px}$ using $20\times$ magnification. An iterative labeling process was employed, beginning with automatic labeling, followed by semi-automatic refinement, and concluding with manual boundary

refinement. This process resulted in the annotation of 418,935 nuclei (we excluded TCGA and PanNuke), classified into neutrophils, lymphocytes, plasma cells, eosinophils, epithelial cells, and connective tissue cells (see S7). The dataset comprises 270 tiles of varying sizes, with an average dimension of $1,016 \times 917$ px (Graham et al., 2021). To process the Lizard dataset with CellViT⁺⁺, the input images were rescaled to $0.25 \mu\text{m}/\text{px}$ using Lanczos resampling, and the output was subsequently rescaled back to $0.50 \mu\text{m}/\text{px}$ prior to performance metric calculations. This procedure enabled the evaluation of the network's ability to generalize across different magnifications. The evaluation was conducted using 3-fold CV based on the splits provided in the original paper, with the PanNuke images excluded for the CellViT⁺⁺ evaluation, due to prior network pretraining. Since the TCGA test set is not publicly available, no external evaluation could be conducted. Similar to CoNSeP, this dataset provides cell-level segmentation masks.

NuCLS. The NuCLS dataset is a crowdsourced collection of nuclei annotations from breast cancer tissue (source TCGA), annotated by medical students and pathologists (Amgad et al., 2022). It contains over 220,000 annotations, with varying levels of quality depending on the extent of pathologist involvement. Specifically, some parts of the dataset were annotated by medical students who had access to pathologist feedback, though the final annotations were not always reviewed by a pathologist (lower quality). Other subsets of the dataset were annotated by multiple non-experts and experts to enhance reliability. For this study, we utilized the corrected single-rater subset, which represents the highest quality control level within the NuCLS dataset (Amgad et al., 2022). This subset includes annotations that have been corrected under the direct supervision of a pathologist. The training data comprises 124 whole slide images (WSIs), divided into 5 folds, with 15 WSIs reserved for testing. For each WSI, multiple crops have been annotated. Each crop has a resolution of $0.20 \mu\text{m}/\text{px}$. Annotations in the crops are provided within a field of view area as either fine-grained cell contours or bounding boxes. If a nucleus extends beyond the FOV boundary, its boundary or bounding box is extended into the surrounding area of the crop. Each FOV has an average width and height of 320 pixels, corresponding to a field size of approximately $65 \times 65 \mu\text{m}$. The FOVs were annotated at high magnification to accurately indicate the location and classification of all nuclei within the area. For our analysis, we cut out the FOV area (320 px) from the crops and resized them to 256×256 px, resulting in a resolution of $0.25 \mu\text{m}/\text{px}$. We included only those cells whose center of mass fell within the FOV region. Additionally, we removed ambiguous nuclei labels. This process reduced the original dataset from 59,485 nuclei to 48,365 nuclei. An overview of the final dataset size and the distribution of nuclei among the main and super annotation classes is provided in the Supplementary Table S11.

The primary classes analyzed in our study include lymphocytes and plasma cells (superclass: sTILs), macrophages and stromal cells (superclass: stromal cells), mitotic and non-mitotic tumor cells (superclass: tumor cells), and miscellaneous cells. Our evaluation focuses on the performance of classifiers on these main classes within the NuCLS dataset. Additionally, we use the NuCLS test set to compare the performance of CellViT⁺⁺ classifiers trained on the automatically derived SegPath dataset described below. For this comparison, we establish baseline results by training classifiers specifically on the lymphocyte and plasma cell classes, changing the tasks to a binary classification problem for each cell class, determining whether a cell belongs to the class or not.

PanopTILs. Introduced by Liu et al. (2024), the PanopTILs dataset provides region and cell-level annotations for 859,759 nuclei from 151 breast cancer patients within the TCGA cohort. The dataset is particularly significant due to its focus on TILs, which hold substantial prognostic and predictive value in breast cancer. Despite their clinical importance, the visual assessment of TILs is highly subjective. Computational TIL scores have been shown to possess a higher prognostic value than traditional visual assessments, independent of TNM stage and patient age. This underscores the clinical relevance of the PanopTILs dataset and highlights its potential as a valuable resource for analyzing the breast tumor microenvironment (Liu et al., 2024). The dataset comprises annotations for several cell types, including TILs, stromal cells, epithelial cells, and

miscellaneous cells, grouped according to the classification scheme suggested by Liu et al. (2024). Although the dataset also includes region-wise annotations, our analysis focused solely on the nuclei labels.

The PanopTILs dataset is divided into two parts: one for training and validation, and the other for testing. Training data includes manually defined regions with algorithmically bootstrapped nuclei labels, while the test set features manual regions with pathologist-approved nuclei annotations. In total, the training dataset consists of 1,709 image crops, each measuring $1,024 \times 1,024$ px, containing 814,886 annotated cells. The test set, derived from the NuCLS dataset, includes only cells within a field of view (FOV), which is smaller than the $1,024 \times 1,024$ px crop size used in the training data. Consequently, the evaluation of the test data is performed only on these FOV segments, not on the entire crops. The test set consists of 1,317 crops with 44,873 annotated cells. All images have a resolution of $0.25 \mu\text{m}/\text{px}$ at $\times 40$ magnification. As a newly introduced dataset, PanopTILs provides a novel benchmark for the evaluation of cell detection performance, specifically within the context of breast cancer microenvironment analysis. Unlike prior studies (Liu et al., 2024) that primarily focused on the classification accuracy of detected cells, our work contributes by establishing baseline results for TIL detection using PanopTILs.

SegPath. The SegPath (Komura et al., 2023) dataset has a substantial difference to the previously listed datasets, as it is not a conventional annotated cell dataset. Unlike traditional datasets, where ground truth segmentation masks are manually derived from pathologists' annotations, SegPath's segmentation masks were automatically generated through the registration of IF stainings. Indeed, the dataset does not provide cell level segmentations, but rather region-wise segmentation masks. It was developed for the semantic segmentation of H&E stained images, specifically focusing on eight major cell types within tumor tissues. The dataset acquisition process was fully automated. First, tissue sections were stained with H&E and subsequently digitized using a slide scanner. These sections were then destained through alcohol and autoclave processing, followed by IF staining with 4',6-diamidino-2-phenylindole dihydrochloride (DAPI) nuclear staining (Komura et al., 2023). Specific antibodies were used to identify each cell type. The slides were digitized again after IF staining. To ensure precise alignment of the hematoxylin component in the H&E images with the DAPI channel in the IF images, multiresolution rigid and non-rigid registration steps were applied. Binary segmentation masks were then generated based on the IF intensity, followed by morphological erosion (Komura et al., 2023). With this procedure, the authors were able to create a dataset consisting of 158,687 registered H&E and IF patches, each with a size of 984×984 pixels at a resolution of $0.22 \mu\text{m}/\text{px}$ at $\times 40$ magnification. The dataset includes segmentation masks for epithelium (antibody: Pan-cytokeratin), smooth muscle/myofibroblast (antibody: αSMA), lymphocytes (antibodies: CD3/CD20), leukocytes (antibody: CD45RB), blood/lymphatic vessels (antibody: ERG), plasma cells (antibody: MIST1), myeloid cells (antibody: MNDA), and red blood cells (antibody: CD235a) across 20 different organs. However, it does not contain cell-level instance segmentations. To derive a cell-level dataset of the H&E-slides from the antibody IF segmentation masks, we applied CellViT⁺⁺ to the H&E patches and transferred the segmentation results onto the IF masks. A cell was considered positive if the detected cell had more than 15% overlap with the antibody mask; otherwise, it was assigned the negative class label. This allows for the rapid creation of large-scale cell datasets. A critical aspect of this method is the selection of antibodies with high specificity. The chosen antibody must effectively stain the nuclei while avoiding excessive staining of cytoplasm areas. The antibodies CD3/CD20 (for lymphocytes) and MIST1 (for plasma cells) proved particularly suitable, as they distinctly marked the nuclei and provided clear nuclear staining. To assess the performance of classifiers trained on these automatically derived cell datasets, we focused on the breast cancer subset of SegPath, specifically targeting lymphocyte and plasma cell data. The classifiers were trained on this subset and evaluated using the test set from the NuCLS dataset, which includes manual annotations supervised by pathologists. Using the CellViT⁺⁺ approach, we extracted over 5,000 lymphocyte cells from 220 H&E patches and 27,000 plasma cells from 2,054 patches within the SegPath training

dataset for breast cancer, on which the classifiers can be trained.

Metrics

Nuclei Detection. To evaluate the performance of the model for the case of cell detection, we applied the metrics precision, recall, and F_1 -score. Given that the detection of cells also involves classifying the cells into the correct cell class, our calculations account for the correct assignment of classes. The scores are first computed separately for each class and then averaged across them. Following the approach of [Ryu et al. \(2023\)](#), these metrics are referred to as mean precision (mPrec), mean recall (mRec), and mean F_1 -score (mF₁). In the context of cell detection, the metrics can be interpreted as follows. Precision measures the accuracy of the detected cells relative to the ground truth. It is defined as the ratio of true positive (TP) detections (i.e., correctly detected cells with corresponding ground-truth (GT)) to the total number of cells detected by the model including both TP and false positives (FP). False positive cells are cells that do not match any GT cell. A high precision indicates that most of the detected cells are correct, with a low amount of FP cells. Conversely, if precision is low, the model detects many FP cell are indeed not present in the specimen. Recall, on the other hand, measures the model’s ability to detect cells in the specimen. It is defined as the ratio of the TP cells to the the total number of cells in the ground-truth of the slide indicated by the sum of TP and false negatives (FN). Models with a high recall detect most of the present cells, whereas models with a low recall miss many cells. The F_1 -Score combines precision and recall by calculating the harmonic mean of both metrics. It is a preferred metric in many classification and detection tasks because it effectively balances the trade-off between precision and recall to capture both aspects.

In the case of cell detection, the challenge remains in determining when a cell can be considered detected. To ensure consistency with previous works, we adopt the approach of [Ryu et al. \(2023\)](#). A predicted cell is considered as TP if an annotated cell of the same class is within a distance of 15 pixels, i.e., 3 – 4 μm depending on the baseline resolution (0.20 – 0.27 $\mu\text{m}/\text{px}$ at $\times 40$ magnification). Otherwise, the detected cell is considered FP. If an annotated cell cannot be matched to a prediction, it is considered a FN cell. To calculate the mF₁-score, each cell class score is calculated with

$$F_1 = 2 \times \frac{\text{Precision} \times \text{Recall}}{\text{Precision} + \text{Recall}}$$

$$\text{Precision} = \frac{\text{TP}}{\text{TP} + \text{FP}}$$

$$\text{Recall} = \frac{\text{TP}}{\text{TP} + \text{FN}}$$

Further details on the algorithmic implementation can be found in the original publication on the Ocelot dataset ([Ryu et al., 2023](#)).

Nuclei Instance Segmentation. The detection metrics described above, while well-suited for comparing the classification and detection quality of networks, are insufficient for assessing the segmentation quality of cells. For many applications, it is crucial that the contours of cells are accurately captured, particularly for algorithms that rely on classical cell features. Therefore, in addition to the precision, recall, and F_1 -score metrics, it is necessary to include metrics that reflect segmentation quality. In this study, we use the Panoptic Quality (PQ), specifically the binary PQ (bPQ) and mean PQ (mPQ) introduced by [Graham et al. \(2019b\)](#). These metrics consider both the segmentation quality of each nucleus and the quality of distinguishing between nuclei, including their class assignment. It is defined as

$$PQ = \underbrace{\frac{|TP|}{|TP| + \frac{1}{2}|FP| + \frac{1}{2}|FN|}}_{\text{Detection Quality (DQ)}} \times \underbrace{\frac{\sum_{(y,\hat{y}) \in TP} IoU(y,\hat{y})}{|TP|}}_{\text{Segmentation Quality (SQ)}}.$$

In this equation $IoU(y, \hat{y})$ denotes the intersection-over-union, with y being a GT segment \hat{y} a predicted segment ([Kirillov et al., 2019](#); [Hörst et al., 2024a](#)). The calculation of true positives (TP), false positives (FP), and false negatives (FN) follows the same principles as for the detection metrics.

For bPQ, it is assumed that all cells belong to the same class, allowing for an assessment of how well nuclei are detected and segmented. The mPQ, in contrast, also considers the class assignment of the nuclei. We utilize the implementation provided in the original HoVer-Net publication ([Graham et al., 2019b](#); [Hörst et al., 2024a](#)). Since the mPQ score is calculated by first determining the PQ value for each image and each class before averaging, this approach can lead to certain classes being excluded from the results if they were predicted but not present in image annotations. This limitation arises from the inherent calculation method described by [Graham et al. \(2019b\)](#). To address this issue, they introduced the mPQ+ metric, which calculates the metrics across all images first and then averages them by class ([Graham et al., 2023](#)). This modification ensures that all classes are accounted for, regardless of their presence in the ground truth annotations. To avoid confusion, we explicitly specify whether the mPQ or mPQ+ metrics is being reported in our results. We consistently use the metric employed in the original dataset publication to ensure the comparability of our results with comparative methods.

Carbon footprint calculation

The Carbon footprint and energy consumption estimations were conducted using the [Machine Learning Impact calculator](#) presented in [Lacoste et al. \(2019\)](#). Experiments were conducted on a private infrastructure with an estimated carbon efficiency of 0.432 kg CO₂ eq/kWH (OECD’s 2014 yearly average). For HoVer-Net on the CoNSeP dataset, we used the baseline configuration of 2 NVIDIA GeForce 1080 Ti GPUs, trained for 380 minutes (6.3 hours), resulting in an energy consumption of 3,170 WH (equivalent to 1.37 kg CO₂ eq). This setup was scaled for the Lizard dataset, leading to a runtime of 28 hours and an energy consumption of approximately 14,000 WH (6.04 kg CO₂ eq). Using our hardware, for training on the CoNIC dataset, a cropped subset of the Lizard dataset prepared for HoVer-Net, we conducted training for 7.5 hours, consuming 3,000 WH (1.30 kg CO₂ eq), while training on the CoNSeP dataset took 102 minutes (1.7 hours), resulting in 680 WH (0.29 kg CO₂ eq).

Pretraining the largest CellViT model (ViT-H encoder) on the PanNuke dataset with a single NVIDIA A100 80GB GPU for 30 hours resulted in an energy consumption of 12,000 WH (5.18 kg CO₂ eq). However, as demonstrated in our study, the model is a generalized cell segmentation model that can be adapted for new datasets by fine-tuning only the cell classification module based on the tokens. On average across all dataset, fine-tuning the cell classification module under the same setup took 20 minutes, including caching during the first epoch, consuming 120 WH (0.05 kg CO₂ eq). Since the initial caching costs are incurred only during the first epoch in the first run, energy-efficient hyperparameter tuning can be performed, with an accumulated CO₂ equivalent of 0.92 kg (2,120 WH) for 100 experiments. We also determined specific values for the CoNSeP and Lizard datasets. Training the cell classification module took only 81 seconds on an NVIDIA A100 GPU, consuming 9.23 WH with a CO₂ equivalent of 4 gr, which is negligible. For the Lizard dataset, the process took 12 minutes, consuming 92.16 WH (40 gr CO₂ eq). As [Patterson et al. \(2021\)](#) highlighted, the development of a machine learning model consumes far more resources than the final training run, leading to a significantly higher overall energy consumption - a factor we attempt to address by simulating 100 training runs. This analysis shows that, even compared to a parameter-efficient cell segmentation method like HoVer-Net, our energy consumption is substantially reduced.

However, the carbon footprint of foundation models should not be overlooked. Thus, for transparency, we have also calculated the respective carbon footprint of the original publications. The SAM-H model was trained for 68 hours on 256 NVIDIA A100 80GB GPUs, consuming 6,963 kWh (3,008 kg CO₂ eq). Unfortunately, data for the Virchow and Virchow₂ models are not available, but we estimate that at least 48 NVIDIA V100 32GB GPUs were used for 200 hours (based on [Wang et al. \(2022\)](#)), leading to a lower-bound estimate of 3,600 kWh (1,555 kg CO₂ eq). The UNI model was trained with 4×8 Nvidia A100 80GBGPUs for 32 hours, consuming 410 kWh (177 kg CO₂ eq). Despite the significant carbon footprint, foundation models provide substantial advantages in terms

of efficiency and versatility. When these models are fine-tuned and reused across multiple tasks, the overall carbon footprint can be significantly reduced compared to re-training specialized models from scratch for each new application.

Software

The CellViT code, as initially described in Hörst et al. (2024a), was modified to enhance both inference speed and the flexibility of the encoder network, allowing for the integration of the Virchow and Virchow₂ ViT architectures. During inference, the tool for slide processing is Pathopatch (v. 1.0.4b0), which integrates OpenSlide (v. 4.0.0), wsidicom (v. 0.20.4), and CUCIM (v. 24.04.00). This combination of tools allowed us to preprocess slides from a variety of open-source and vendor formats, including DICOM. All experiments and analyses were conducted using Python (v. 3.10.14). The reproducibility of these experiments is ensured through the use of open-source libraries, with the most important libraries specified as follows: PyTorch (v. 2.2.1) along with its associated libraries torchvision (v. 0.17.1) and torchmetrics (v. 0.11.4), numpy (v. 1.23.5), numba (v. 0.59.0), CuPY (v. 13.0.0), CUCIM (v. 24.04.00), OpenSlide (v. 4.0.0), pandas (v. 1.4.3), scikit-learn (v. 1.3.0), PyCaret (v. 3.3.2) and CatBoost (v. 1.2.5). The implementations of the foundation Models used in this study were sourced from the following repositories: UNI, available at <https://huggingface.co/MahmoodLab/UNI>; Virchow, available at <https://huggingface.co/paige-ai/Virchow>; Virchow2, available at <https://huggingface.co/paige-ai/Virchow2>; HIPT, available at <https://github.com/mahmoodlab/HIPT>; and Segment Anything, available at <https://github.com/facebookresearch/segment-anything>. A full list is given in the Supplementary Table S22.

Data availability

The study is based on public available datasets. The datasets have been acquired from the following sources: Ocelot (Ryu et al., 2023), available at <https://ocelot2023.grand-challenge.org/>; Midog ++ (Aubreville et al., 2023), available at <https://doi.org/10.6084/m9.figshare.c.6615571.v1>; CoNSeP (Graham et al., 2019b), available at https://warwick.ac.uk/fac/cross_fac/tia/data/; Lizard (Graham et al., 2021), available at https://warwick.ac.uk/fac/cross_fac/tia/data/; NuCLS (Amgad et al., 2022), available at <https://sites.google.com/view/nucls/>; SegPath (Komura et al., 2023) available at <https://dakomura.github.io/SegPath/>; and PanopTILs (Liu et al., 2024) available at <https://sites.google.com/view/panoptils/>. A full list is given in the Supplementary Table S21.

Code availability

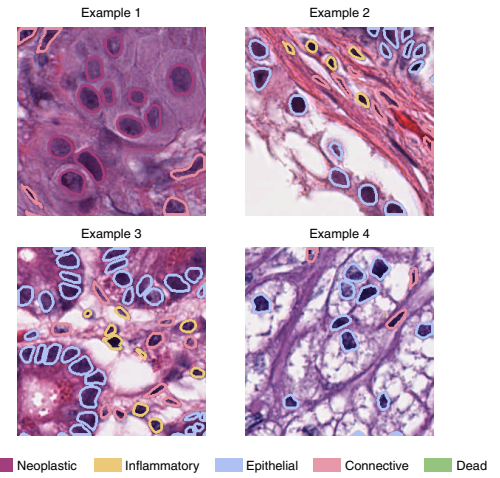
The source code of CellViT⁺⁺ is available at <https://github.com/TIO-IKIM/CellViT-plus-plus>.

Extended Data Figures

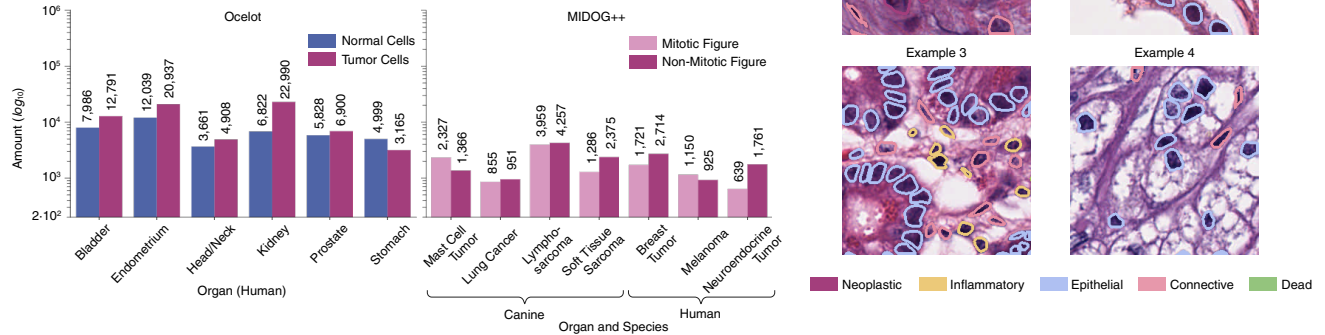
a CellViT Segmentation Results after Pretraining on the PanNuke Dataset

	CellViT _{ViT-S}	CellViT _{HIP1256}	CellViT _{LIN}	CellViT _{Vichow}	CellViT _{Vichow2}	CellViT _{SAM-H}
bPQ	0.6264 ± 0.0399	0.6696 ± 0.0340	0.6642 ± 0.0351	0.6649 ± 0.0338	0.6652 ± 0.0327	0.6793 ± 0.0318
mPQ	0.4417 ± 0.0500	0.4846 ± 0.0503	0.4917 ± 0.0415	0.4893 ± 0.0385	0.4926 ± 0.0384	0.4980 ± 0.0413

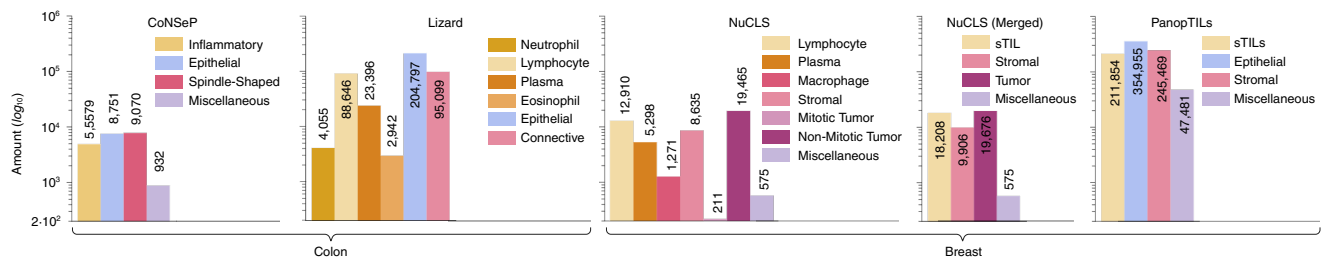
b Example Images of the PanNuke dataset



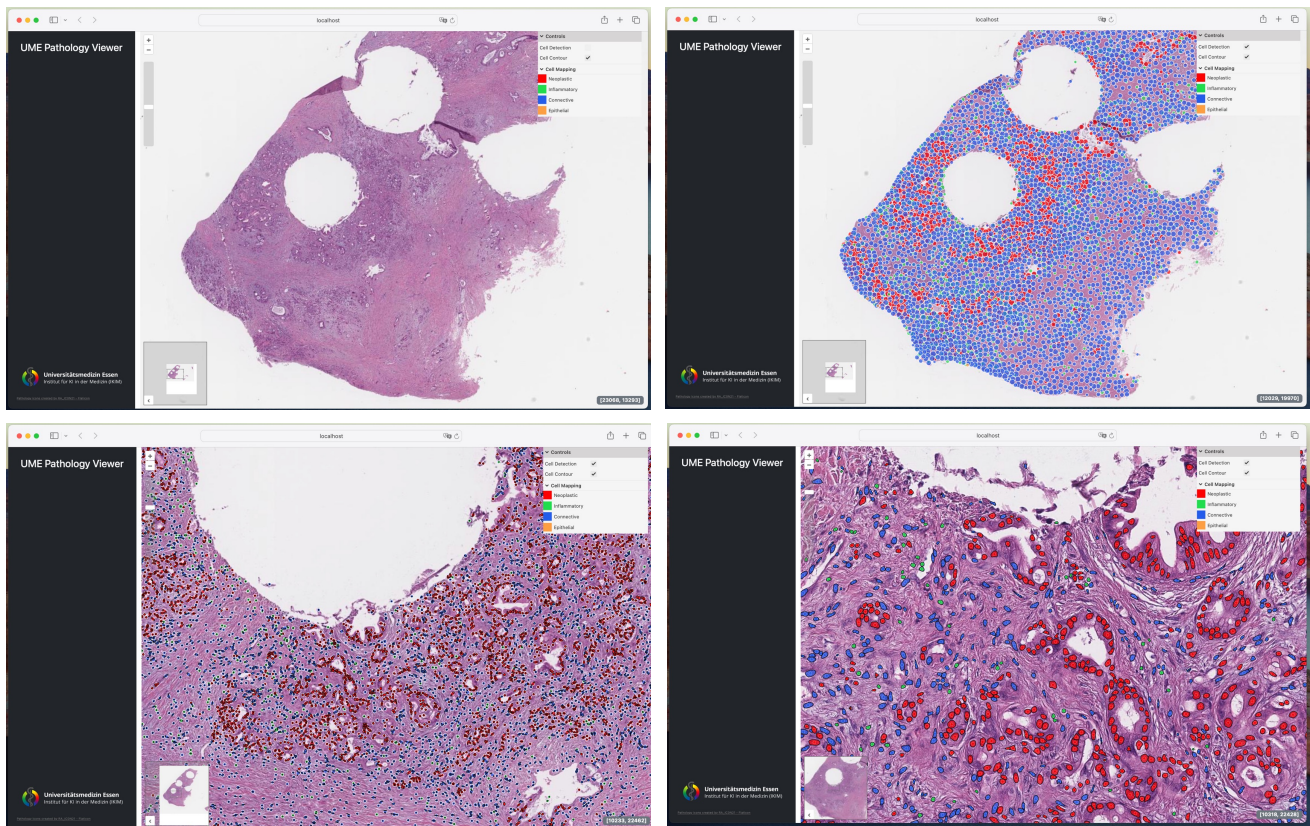
c Multi-Organ Nuclei Datasets



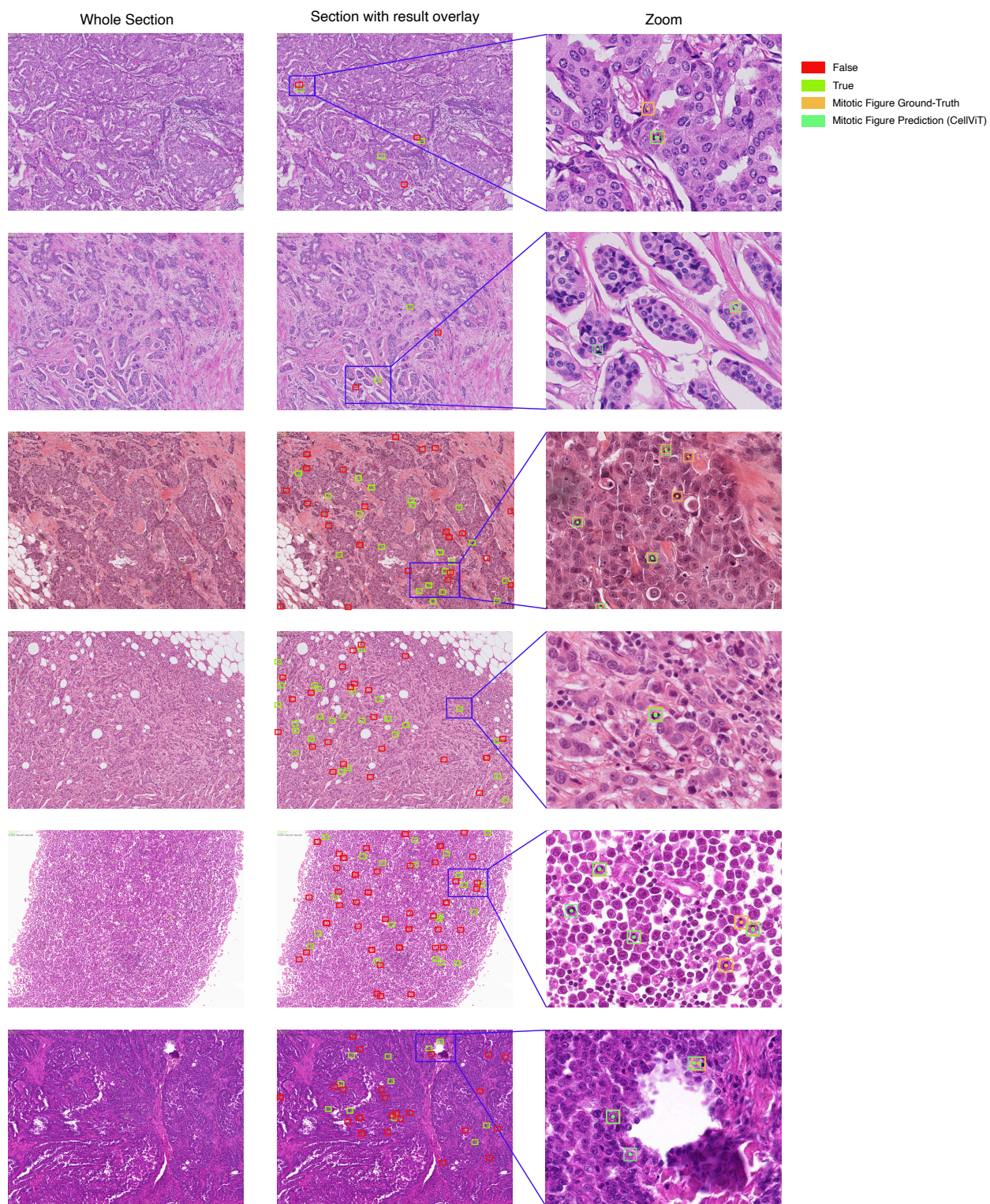
d Single-Organ Nuclei Datasets



Extended Data Fig. 1. Pretraining results and overview of the datasets used in our work. **a** Panoptic quality (PQ) of each CellViT⁺⁺ Variant on the PanNuke dataset using different foundation models as image encoders. Metrics are splitted into binary PQ (bPQ) and mean PQ (mPQ) taking the PanNuke nuclei classification into account. **b** Example training patches (256 × 256 px) for the segmentation heads of the PanNuke dataset. **c** Multi organ nuclei datasets for tumor cell detection (Ocelot) and mitosis detection (MIDOG++). **d** Single organ datasets. We compared our models extensively on cells from two organs: Breast and colon.



Extended Data Fig. 2. New web-based WSI viewer demonstrating visualization capabilities without local software installation using modern web technologies. (Upper left) General overview of the WSI. (Upper right) Overview with cell detections, clustered to depict spatial distribution. (Lower left) Zoomed-in view of a selected region with detailed cell detections. (Lower right) High-resolution view with cell contour overlays.



Extended Data Fig. 3. Representative tissue sections from the MIDOG++ dataset, illustrating the challenge of mitotic figure detection as a "needle in a haystack" problem. Each WSI section is annotated with ground truth (GT) mitotic figures and corresponding predictions generated by the CellViT_{SAM-H}⁺⁺ model.

Supplementary Tables

Table S1. Average mPQ and bPQ scores across the 19 tissue types of the PanNuke dataset for 3-fold CV for all CellViT variants. The standard deviation (SD) of the splits is provided in the final row. Best results are marked bold, second best underlined.

Tissue	CellViT _{HIPT₂₅₆}		CellViT _{UNI}		CellViT _{Virchow}		CellViT _{Virchow₂}		CellViT _{SAM-H}	
	<i>mPQ</i>	<i>bPQ</i>	<i>mPQ</i>	<i>bPQ</i>	<i>mPQ</i>	<i>bPQ</i>	<i>mPQ</i>	<i>bPQ</i>	<i>mPQ</i>	<i>bPQ</i>
Adrenal	0.4950	<u>0.7009</u>	0.5033	0.6939	<u>0.5087</u>	0.6979	0.5028	0.6960	0.5134	0.7086
Bile Duct	0.4721	<u>0.6705</u>	0.4736	0.6592	0.4763	0.6643	<u>0.4820</u>	0.6729	0.4887	0.6784
Bladder	0.5756	<u>0.7056</u>	<u>0.5789</u>	0.6980	0.5599	0.6958	<u>0.5595</u>	0.6898	0.5844	0.7068
Breast	<u>0.5089</u>	<u>0.6641</u>	0.5006	0.6547	0.4999	0.6562	0.5043	0.6563	0.5180	0.6748
Cervix	<u>0.4893</u>	<u>0.6862</u>	<u>0.4911</u>	0.6815	0.4908	0.6766	0.4849	0.6724	0.4984	0.6872
Colon	0.4245	0.5700	0.4392	0.5729	<u>0.4398</u>	<u>0.5730</u>	0.4377	0.5728	0.4485	0.5921
Esophagus	<u>0.5373</u>	<u>0.6619</u>	0.5267	0.6525	0.5352	0.6573	0.5325	0.6544	0.5454	0.6682
Head & Neck	0.4901	<u>0.6472</u>	0.4827	0.6316	0.4709	0.6361	<u>0.4904</u>	0.6395	0.4913	0.6544
Kidney	0.5409	0.6993	0.5610	<u>0.7094</u>	0.5483	0.6940	<u>0.5602</u>	0.6975	0.5366	0.7092
Liver	0.5065	0.7160	<u>0.5140</u>	<u>0.7180</u>	0.5078	<u>0.7180</u>	0.5111	0.7158	0.5224	0.7322
Lung	0.4102	<u>0.6317</u>	<u>0.4235</u>	0.6250	0.4228	0.6205	0.4314	0.6308	0.4314	0.6426
Ovarian	<u>0.5260</u>	0.6596	0.5218	0.6564	0.5185	0.6529	0.5207	<u>0.6620</u>	0.5390	0.6722
Pancreatic	<u>0.4769</u>	<u>0.6643</u>	0.4723	0.6530	0.4700	0.6604	0.4924	0.6626	0.4719	0.6658
Prostate	0.5164	<u>0.6695</u>	<u>0.5247</u>	0.6666	0.5169	0.6682	0.5182	0.6640	0.5321	0.6821
Skin	0.3661	0.6400	0.4342	0.6320	0.4442	<u>0.6425</u>	<u>0.4384</u>	0.6327	0.4339	0.6565
Stomach	<u>0.4475</u>	<u>0.6918</u>	0.4463	0.6896	0.4354	0.6827	0.4405	0.6851	0.4705	0.7022
Testis	<u>0.5091</u>	<u>0.6883</u>	0.5024	0.6760	0.5046	0.6794	0.5044	0.6758	0.5127	0.6955
Thyroid	0.4412	0.7035	0.4596	0.7018	0.4630	<u>0.7080</u>	<u>0.4598</u>	0.7056	0.4519	0.7151
Uterus	0.4737	0.6516	<u>0.4863</u>	0.6481	0.4838	0.6497	0.4873	<u>0.6526</u>	0.4737	0.6625
Average	0.4846	<u>0.6696</u>	0.4917	0.6642	0.4893	0.6649	<u>0.4926</u>	0.6652	0.4980	0.6793
SD	0.0503	0.0340	0.0415	0.0351	0.0385	0.0338	0.0384	0.0327	0.0413	0.0318

Table S2. CellViT-Backbone comparison (mPQ) on the PanNuke dataset, split by cell-type. Average results of the official 3-fold CV split. Best results are marked bold, second best underlined.

Model	Neoplastic	Epithelial	Inflammatory	Connective	Dead
CellViT _{HIPT₂₅₆}	0.567	0.559	<u>0.405</u>	0.405	0.144
CellViT _{UNI}	0.573	0.579	<u>0.403</u>	0.408	<u>0.152</u>
CellViT _{Virchow}	0.577	<u>0.580</u>	0.393	0.409	0.147
CellViT _{Virchow₂}	<u>0.578</u>	<u>0.580</u>	0.403	<u>0.410</u>	0.154
CellViT _{SAM-H}	0.581	0.583	0.417	0.423	0.149

Table S3. Overview of the Ocelot dataset splits and amount of nuclei for the training, validation and test split.

Amount	Training						Validation	Test
	5%	10%	25%	50%	75%	100%		
Tumor Cells	1,571	5,056	12,607	22,994	32,766	42,505	16,312	12,874
Non-Tumor Cells	1,644	2,579	5,966	10,695	17,982	23,332	8,400	9,603
Total	3,215	7,635	18,573	33,689	50,748	65,837	24,712	22,477

Table S4. Average F_1 -score of the baseline model (SoftCTM) and the best-performing CellViT⁺⁺ model (CellViT⁺⁺_{SAM-H}) across different training data sizes, averaged over 5 runs. The performance of CellViT⁺⁺_{SAM-H} is evaluated with and without data augmentation, with results provided for each organ along with the standard deviation.

Amount	Organ	Bladder	Endometrium	Head & Neck	Kidney	Prostate	Stomach	Average
	Network	$F_1 \pm SD$	$F_1 \pm SD$	$F_1 \pm SD$	$F_1 \pm SD$	$F_1 \pm SD$	$F_1 \pm SD$	$mF_1 \pm SD$
5%	SoftCTM	0.2488 ± 0.0928	0.2532 ± 0.0969	0.1820 ± 0.0916	0.3388 ± 0.1403	0.1987 ± 0.0668	0.2458 ± 0.1144	0.2692 ± 0.1105
	CellViT ⁺⁺ _{SAM-H}	0.5854 ± 0.0084	0.6875 ± 0.0070	0.5758 ± 0.0072	0.5575 ± 0.0120	0.6269 ± 0.0116	0.6224 ± 0.0108	0.6291 ± 0.0065
	CellViT ⁺⁺ _{SAM-H} (Aug)	0.5901 ± 0.0140	0.6870 ± 0.0186	0.5750 ± 0.0152	0.5731 ± 0.0256	0.6499 ± 0.0104	0.6329 ± 0.0156	0.6362 ± 0.0082
10%	SoftCTM	0.5783 ± 0.0170	0.6355 ± 0.0223	0.5639 ± 0.0303	0.5932 ± 0.0115	0.5599 ± 0.0178	0.6543 ± 0.0182	0.6100 ± 0.0173
	CellViT ⁺⁺ _{SAM-H}	0.5988 ± 0.0039	0.7104 ± 0.0061	0.5894 ± 0.0088	0.5931 ± 0.0069	0.6392 ± 0.0090	0.6589 ± 0.0080	0.6507 ± 0.0035
	CellViT ⁺⁺ _{SAM-H} (Aug)	0.5735 ± 0.0244	0.7181 ± 0.0086	0.5707 ± 0.0094	0.6005 ± 0.0177	0.6503 ± 0.0176	0.6749 ± 0.0084	0.6507 ± 0.0092
25%	SoftCTM	0.6693 ± 0.0084	0.7019 ± 0.0084	0.6176 ± 0.0312	0.6339 ± 0.0099	0.6340 ± 0.0093	0.7090 ± 0.0169	0.6736 ± 0.0037
	CellViT ⁺⁺ _{SAM-H}	0.6046 ± 0.0133	0.6964 ± 0.0111	0.5997 ± 0.0087	0.6081 ± 0.0157	0.6356 ± 0.0053	0.7080 ± 0.0084	0.6550 ± 0.0073
	CellViT ⁺⁺ _{SAM-H} (Aug)	0.6091 ± 0.0066	0.7056 ± 0.0042	0.5574 ± 0.0176	0.6074 ± 0.0142	0.6371 ± 0.0223	0.7047 ± 0.0108	0.6539 ± 0.0073
50%	SoftCTM	0.6797 ± 0.0051	0.7195 ± 0.0067	0.5385 ± 0.0272	0.6573 ± 0.0060	0.6619 ± 0.0096	0.7425 ± 0.0058	0.6820 ± 0.0048
	CellViT ⁺⁺ _{SAM-H}	0.6287 ± 0.0132	0.7123 ± 0.0110	0.6041 ± 0.0121	0.6327 ± 0.0109	0.6594 ± 0.0083	0.6968 ± 0.0043	0.6695 ± 0.0072
	CellViT ⁺⁺ _{SAM-H} (Aug)	0.6378 ± 0.0093	0.7160 ± 0.0060	0.5734 ± 0.0271	0.6457 ± 0.0170	0.6635 ± 0.0208	0.6994 ± 0.0078	0.6716 ± 0.0073
75%	SoftCTM	0.6899 ± 0.0094	0.7387 ± 0.0065	0.6001 ± 0.0333	0.6775 ± 0.0092	0.6384 ± 0.0286	0.7623 ± 0.0046	0.6986 ± 0.0038
	CellViT ⁺⁺ _{SAM-H}	0.6089 ± 0.0069	0.7168 ± 0.0058	0.6307 ± 0.0143	0.6235 ± 0.0121	0.6437 ± 0.0142	0.6950 ± 0.0089	0.6669 ± 0.0054
	CellViT ⁺⁺ _{SAM-H} (Aug)	0.6293 ± 0.0071	0.7214 ± 0.0036	0.5898 ± 0.0192	0.6280 ± 0.0108	0.6544 ± 0.0173	0.6940 ± 0.0093	0.6694 ± 0.0053
100%	SoftCTM	0.6955 ± 0.0094	0.7459 ± 0.0074	0.6267 ± 0.0268	0.6779 ± 0.0207	0.6850 ± 0.0377	0.7660 ± 0.0066	0.7109 ± 0.0069
	CellViT ⁺⁺ _{SAM-H}	0.6276 ± 0.0085	0.7338 ± 0.0028	0.6359 ± 0.0095	0.6532 ± 0.0120	0.6542 ± 0.0091	0.7049 ± 0.0120	0.6827 ± 0.0028
	CellViT ⁺⁺ _{SAM-H} (Aug)	0.6225 ± 0.0148	0.7311 ± 0.0076	0.6078 ± 0.0173	0.6374 ± 0.0106	0.6493 ± 0.0152	0.6825 ± 0.0110	0.6726 ± 0.0080

Table S5. Average F_1 -score and standard deviation (SD) of the baseline model (SoftCTM) and all CellViT⁺⁺ variants averaged over 5 runs when 100% of the training data is used for the Ocelot dataset.

Network	Organ	Bladder	Endometrium	Head & Neck	Kidney	Prostate	Stomach	Average
	Data Augmentation	$F_1 \pm SD$	$F_1 \pm SD$	$F_1 \pm SD$	$F_1 \pm SD$	$F_1 \pm SD$	$F_1 \pm SD$	$mF_1 \pm SD$
SoftCTM	Yes	0.6955 ± 0.0094	0.7459 ± 0.0074	0.6267 ± 0.0268	0.6779 ± 0.0207	0.6850 ± 0.0377	0.7660 ± 0.0066	0.7109 ± 0.0069
CellViT ⁺⁺ _{HIPT₂₅₆}	No	0.5832 ± 0.0023	0.7129 ± 0.0028	0.6053 ± 0.0041	0.5809 ± 0.0026	0.6158 ± 0.0030	0.6291 ± 0.0039	0.6426 ± 0.0024
	Yes	0.5855 ± 0.0059	0.7109 ± 0.0065	0.6069 ± 0.0143	0.5820 ± 0.0108	0.6134 ± 0.0055	0.6281 ± 0.0164	0.6425 ± 0.0078
CellViT ⁺⁺ _{UNI}	No	0.6337 ± 0.0020	0.6659 ± 0.0037	0.6399 ± 0.0040	0.6537 ± 0.0021	0.6158 ± 0.0054	0.6586 ± 0.0019	0.6537 ± 0.0019
	Yes	0.6362 ± 0.0054	0.6673 ± 0.0037	0.6426 ± 0.0027	0.6581 ± 0.0032	0.6217 ± 0.0047	0.6598 ± 0.0059	0.6565 ± 0.0022
CellViT ⁺⁺ _{Virchow}	No	0.5775 ± 0.0085	0.6301 ± 0.0048	0.5939 ± 0.0095	0.6058 ± 0.0046	0.5477 ± 0.0056	0.5920 ± 0.0041	0.6073 ± 0.0023
	Yes	0.5930 ± 0.0154	0.6386 ± 0.0071	0.5669 ± 0.0190	0.6091 ± 0.0076	0.5458 ± 0.0131	0.6034 ± 0.0048	0.6113 ± 0.0050
CellViT _{Virchow₂}	No	0.5773 ± 0.0136	0.6541 ± 0.0095	0.5966 ± 0.0141	0.6303 ± 0.0134	0.5477 ± 0.0144	0.5827 ± 0.0051	0.6158 ± 0.0095
	Yes	0.5561 ± 0.0061	0.6457 ± 0.0074	0.5958 ± 0.0200	0.6186 ± 0.0067	0.5438 ± 0.0066	0.5807 ± 0.0092	0.6071 ± 0.0032
CellViT ⁺⁺ _{SAM-H}	No	0.6276 ± 0.0085	0.7338 ± 0.0028	0.6359 ± 0.0095	0.6532 ± 0.0120	0.6542 ± 0.0091	0.7049 ± 0.0120	0.6827 ± 0.0028
	Yes	0.6225 ± 0.0148	0.7311 ± 0.0076	0.6078 ± 0.0173	0.6374 ± 0.0106	0.6493 ± 0.0152	0.6825 ± 0.0110	0.6726 ± 0.0080

Table S6. Overview of the CoNSeP dataset splits and amount of nuclei for the entire training and test split as well as the tile level training subset.

Tile Amount	Nuclei Amount			
	Inflammatory	Epithelial	Spindle-Shaped	Miscellaneous
1	26	223	464	54
2	30	711	714	151
3	308	1,095	1,047	153
4	340	1,095	1,145	168
5	351	1,095	1,145	197
6	446	1,382	1,604	206
7	476	1,660	1,798	206
8	550	1,993	2,128	210
9	550	1,993	2,128	230
10	782	1,993	2,542	231
11	819	2,445	2,592	231
12	852	2,445	2,719	232
13	895	2,445	2,938	232
14	927	3,173	2,974	241
15	2,945	3,173	3,239	241
All Training Tiles	3,941	5,537	5,706	371
All Test Tiles	1,638	3,214	3,364	561

Table S7. Summary of cell annotations present in the Lizard dataset split by cell type and data source. Adopted from [Graham et al. \(2021\)](#).

Type/Dataset	DigestPath	CRAG	GlaS	CoNSeP	Total
Epithelial	70,789	99,124	31,986	2,898	204,797
Lymphocyte	49,932	27,634	9,763	1,317	88,646
Plasma	11,352	9,363	2,349	332	23,396
Neutrophil	2,262	1,673	90	30	4,055
Eosinophil	1,349	1,255	286	52	2942
Connective	32,826	49,994	10,890	1,389	95,099
Total	168,510	189,043	55,364	6,018	418,935

Table S8. Comparison of multiple baseline models on the CoNSeP dataset. All baseline models have been trained on the training set, with subsequent validation on the test set. We report the original publication scores if available, but we also re-trained the networks with the setup described in the original publication. The CellViT⁺⁺ variants have all been trained and validated with 5 fold CV, with final evaluations of each fold on the test set. To estimate the average performance and distribution, we report the mean and standard deviation for our models.

Score Model	Binary Scores							Class-Averaged-Scores					
	F ₁ -Score	DICE	AJI	AJI+	bPQ	bDQ	bSQ	mPQ ± SD	mDQ ± SD	mSQ ± SD	mPQ ± ±SD	mDQ± ± SD	mSQ± ± SD
HoVer-Net (Orig-Publication)	-	0.853	0.571	-	0.547	0.702	0.778	-	-	-	-	-	-
HoVer-Net (PanNuke Baseline)	0.691	0.802	0.492	0.524	0.461	0.609	0.755	-	-	-	-	-	-
HoVer-Net (self-trained)	0.731	0.836	0.535	0.563	0.505	0.656	0.767	0.364	0.463	0.712	0.429	0.550	0.773
Pointnu-Net (self-trained)	0.737	0.782	0.525	0.561	0.522	0.686	0.759	0.383	0.495	0.722	0.446	0.588	0.752
CellViT ⁺⁺ _{HIP256}	0.752	0.815	0.527	0.556	0.504	0.663	0.758	0.344 ± 0.014	0.447 ± 0.017	0.663 ± 0.007	0.398 ± 0.039	0.519 ± 0.053	0.761 ± 0.001
CellViT ⁺⁺ _{JNI}	0.720	0.818	0.525	0.552	0.492	0.649	0.756	0.341 ± 0.009	0.444 ± 0.011	0.669 ± 0.019	0.377 ± 0.026	0.491 ± 0.036	0.722 ± 0.073
CellViT ⁺⁺ _{Virchow}	0.722	0.808	0.493	0.511	0.451	0.607	0.741	0.329 ± 0.009	0.432 ± 0.011	0.667 ± 0.006	0.386 ± 0.027	0.511 ± 0.038	0.749 ± 0.002
CellViT ⁺⁺ _{Virchow₂}	0.725	0.811	0.493	0.513	0.457	0.612	0.743	0.331 ± 0.013	0.436 ± 0.016	0.675 ± 0.018	0.359 ± 0.023	0.474 ± 0.032	0.750 ± 0.007
CellViT ⁺⁺ _{SAM-H}	0.772	0.845	0.578	0.608	0.548	0.709	0.771	0.397 ± 0.004	0.507 ± 0.006	0.675 ± 0.008	0.461 ± 0.014	0.596 ± 0.018	0.768 ± 0.001

Table S9. CellViT⁺⁺_{SAM-H} performance with and without data augmentation on the CoNSEP dataset. In this experiment, the models have been trained on limited training data, starting from one ROI up to 15 ROIs (compare Tab. S6). We report the performance among all cell types. For comparison, we include the baseline result with 100 % training data in the bottom part.

Num-Files	Data Augmentation	Average	Inflammatory	Epithelium	Spindle-Shaped	Miscellaneous
		mPQ + \pm SD	mPQ + \pm SD	mPQ + \pm SD	mPQ + \pm SD	mPQ + \pm SD
1	No	0.326 \pm 0.015	0.336 \pm 0.040	0.467 \pm 0.003	0.404 \pm 0.002	0.098 \pm 0.020
	Yes	0.316 \pm 0.033	0.258 \pm 0.059	0.444 \pm 0.037	0.383 \pm 0.019	0.180 \pm 0.048
2	No	0.375 \pm 0.015	0.331 \pm 0.048	0.484 \pm 0.005	0.410 \pm 0.006	0.273 \pm 0.016
	Yes	0.357 \pm 0.026	0.235 \pm 0.111	0.479 \pm 0.013	0.392 \pm 0.010	0.322 \pm 0.020
3	No	0.441 \pm 0.007	0.521 \pm 0.021	0.503 \pm 0.002	0.427 \pm 0.002	0.314 \pm 0.012
	Yes	0.441 \pm 0.015	0.527 \pm 0.042	0.496 \pm 0.010	0.425 \pm 0.005	0.317 \pm 0.039
4	No	0.452 \pm 0.005	0.551 \pm 0.013	0.505 \pm 0.000	0.427 \pm 0.002	0.326 \pm 0.012
	Yes	0.441 \pm 0.015	0.531 \pm 0.020	0.503 \pm 0.006	0.426 \pm 0.003	0.304 \pm 0.052
5	No	0.443 \pm 0.016	0.529 \pm 0.027	0.503 \pm 0.005	0.425 \pm 0.004	0.315 \pm 0.034
	Yes	0.453 \pm 0.011	0.552 \pm 0.038	0.507 \pm 0.003	0.426 \pm 0.004	0.329 \pm 0.017
6	No	0.452 \pm 0.007	0.537 \pm 0.017	0.504 \pm 0.002	0.425 \pm 0.003	0.342 \pm 0.008
	Yes	0.460 \pm 0.007	0.552 \pm 0.025	0.509 \pm 0.005	0.428 \pm 0.004	0.352 \pm 0.008
7	No	0.459 \pm 0.006	0.561 \pm 0.018	0.505 \pm 0.002	0.428 \pm 0.001	0.343 \pm 0.008
	Yes	0.453 \pm 0.017	0.554 \pm 0.020	0.506 \pm 0.006	0.429 \pm 0.002	0.323 \pm 0.061
8	No	0.463 \pm 0.006	0.571 \pm 0.017	0.500 \pm 0.005	0.431 \pm 0.001	0.349 \pm 0.007
	Yes	0.459 \pm 0.008	0.553 \pm 0.035	0.509 \pm 0.004	0.431 \pm 0.005	0.344 \pm 0.013
9	No	0.460 \pm 0.005	0.562 \pm 0.013	0.503 \pm 0.007	0.430 \pm 0.004	0.344 \pm 0.010
	Yes	0.464 \pm 0.005	0.565 \pm 0.020	0.508 \pm 0.003	0.432 \pm 0.001	0.350 \pm 0.007
10	No	0.468 \pm 0.004	0.580 \pm 0.012	0.509 \pm 0.001	0.432 \pm 0.001	0.350 \pm 0.006
	Yes	0.470 \pm 0.003	0.587 \pm 0.004	0.511 \pm 0.001	0.435 \pm 0.002	0.348 \pm 0.007
11	No	0.462 \pm 0.002	0.567 \pm 0.012	0.506 \pm 0.005	0.433 \pm 0.002	0.344 \pm 0.005
	Yes	0.469 \pm 0.003	0.580 \pm 0.003	0.511 \pm 0.002	0.433 \pm 0.003	0.353 \pm 0.010
12	No	0.468 \pm 0.002	0.583 \pm 0.010	0.508 \pm 0.002	0.431 \pm 0.003	0.348 \pm 0.007
	Yes	0.470 \pm 0.006	0.584 \pm 0.012	0.511 \pm 0.002	0.434 \pm 0.002	0.349 \pm 0.015
13	No	0.467 \pm 0.003	0.576 \pm 0.015	0.510 \pm 0.001	0.433 \pm 0.001	0.351 \pm 0.008
	Yes	0.465 \pm 0.005	0.564 \pm 0.019	0.511 \pm 0.002	0.433 \pm 0.003	0.351 \pm 0.009
14	No	0.468 \pm 0.003	0.584 \pm 0.009	0.509 \pm 0.003	0.432 \pm 0.002	0.346 \pm 0.013
	Yes	0.470 \pm 0.004	0.580 \pm 0.015	0.510 \pm 0.001	0.434 \pm 0.002	0.356 \pm 0.002
15	No	0.466 \pm 0.004	0.572 \pm 0.018	0.510 \pm 0.001	0.432 \pm 0.002	0.353 \pm 0.006
	Yes	0.473 \pm 0.002	0.592 \pm 0.006	0.509 \pm 0.001	0.432 \pm 0.003	0.357 \pm 0.003
Baselines (100% Train)						
CellViT ⁺⁺ _{SAM-H}	No	0.461 \pm 0.014	0.575 \pm 0.010	0.507 \pm 0.003	0.430 \pm 0.002	0.330 \pm 0.048
CellViT ⁺⁺ _{SAM-H}	Yes	0.442 \pm 0.030	0.587 \pm 0.007	0.501 \pm 0.008	0.432 \pm 0.002	0.247 \pm 0.107
HoVer-Net	Yes	0.429	0.596	0.457	0.381	0.281
PointNu-Net	Yes	0.446	0.596	0.476	0.407	0.307

Table S10. Performance comparison on the Lizard dataset. We included the best available baseline models, all evaluated on a 3-Fold CV split. For our CellViT⁺⁺_{SAM-H} model, we further evaluate the performance when using classical feature engineering for extracting cellular features (histomics), including the 3-layer deep learning classifier and CatBoost. External validation on the test set cannot be conducted, as it remains hidden. HoVer-Net Cerberus refers to the scores published in [Graham et al. \(2023\)](#), whereas HoVer-Net baseline refers to the original scores published by the Lizard authors.

Model	Classifier	Dice \pm SD	bPQ \pm SD	mPQ \pm SD	mPQ+ \pm SD
HoVer-Net (Baseline)		0.828 \pm 0.008	0.624 \pm 0.013	0.396 \pm 0.022	-
HoVer-Net (Cerberus)		-	0.584 \pm 0.014	0.295 \pm 0.018	0.409 \pm 0.027
Cerberus		-	0.612 \pm 0.010	0.358 \pm 0.011	0.425 \pm 0.019
CGIS-CPF		0.889 \pm 0.002	0.660 \pm 0.061	0.421 \pm 0.013	-
CellViT ⁺⁺ _{HIPT₂₅₆}	DL, Token-based	0.767 \pm 0.005	0.513 \pm 0.011	0.252 \pm 0.003	0.272 \pm 0.009
CellViT ⁺⁺ _{UNI}	DL, Token-based	0.752 \pm 0.005	0.503 \pm 0.009	0.279 \pm 0.004	0.293 \pm 0.004
CellViT ⁺⁺ _{SAM-H}	DL, Token-based	0.774 \pm 0.004	0.536 \pm 0.009	0.294 \pm 0.002	0.308 \pm 0.006
CellViT ⁺⁺ _{SAM-H}	DL, Nuclei Features (Histomics)	0.774 \pm 0.004	0.536 \pm 0.009	0.255 \pm 0.004	0.251 \pm 0.003
CellViT ⁺⁺ _{SAM-H}	CatBoost, Nuclei Features (Histomics)	0.774 \pm 0.004	0.536 \pm 0.009	0.255 \pm 0.009	0.255 \pm 0.004

Table S11. NuCLS nuclei amount for the main and super annotation classes within the corrected single annotator dataset used in this study. We excluded ambiguous labelled nuclei, as well as nuclei which center of mass lays outside the annotation field of view.

Main Annotations		Lymphocyte	Plasma	Macrophage	Stromal	Mitotic Tumor	Non-Mitotic Tumor	Uncategorized
Merged Super Annotations		sTILs		Stromal		Tumor		Uncategorized
Main	Train	11,162	4,233	1,153	7,214	167	16,921	291
	Test	1,748	1,065	118	1,421	44	2,544	284
Super	Train	15,395		8,367		17,088		291
	Test	2,813		1,539		2,588		284

Table S12. Averaged (SD) 5-Fold CV results on the NuCLS main label set (15 test WSI). The single-rater corrected dataset (correction by pathologists) has been used to assess performance.

		Lymphocyte	Macrophage	Uncategorized	Plasma Cell	Stromal	Tumor (Non-Mitotic)	Tumor Mitotic
CellViT ⁺⁺ _{HIPT₂₅₆}	F ₁ \pm SD	0.654 \pm 0.029	0.082 \pm 0.056	0.029 \pm 0.033	0.606 \pm 0.082	0.670 \pm 0.009	0.774 \pm 0.011	0.008 \pm 0.016
	Prec \pm SD	0.528 \pm 0.038	0.174 \pm 0.108	0.248 \pm 0.228	0.658 \pm 0.016	0.593 \pm 0.013	0.676 \pm 0.018	0.029 \pm 0.057
	Rec \pm SD	0.861 \pm 0.008	0.054 \pm 0.038	0.016 \pm 0.019	0.578 \pm 0.147	0.769 \pm 0.007	0.905 \pm 0.009	0.005 \pm 0.009
CellViT ⁺⁺ _{UNI}	F ₁ \pm SD	0.670 \pm 0.022	0.239 \pm 0.054	0.567 \pm 0.073	0.570 \pm 0.103	0.689 \pm 0.010	0.801 \pm 0.004	0.134 \pm 0.049
	Prec \pm SD	0.545 \pm 0.030	0.325 \pm 0.060	0.837 \pm 0.074	0.718 \pm 0.059	0.598 \pm 0.028	0.714 \pm 0.013	0.302 \pm 0.102
	Rec \pm SD	0.871 \pm 0.017	0.212 \pm 0.089	0.446 \pm 0.122	0.481 \pm 0.121	0.816 \pm 0.023	0.913 \pm 0.011	0.100 \pm 0.053
CellViT ⁺⁺ _{SAM-H}	F ₁ \pm SD	0.661 \pm 0.016	0.102 \pm 0.034	0.037 \pm 0.027	0.544 \pm 0.087	0.691 \pm 0.006	0.800 \pm 0.008	0.092 \pm 0.092
	Prec \pm SD	0.531 \pm 0.021	0.336 \pm 0.062	0.467 \pm 0.241	0.675 \pm 0.049	0.601 \pm 0.015	0.719 \pm 0.014	0.213 \pm 0.198
	Rec \pm SD	0.878 \pm 0.012	0.061 \pm 0.023	0.020 \pm 0.015	0.463 \pm 0.110	0.814 \pm 0.012	0.902 \pm 0.003	0.059 \pm 0.060

Table S13. Performance of the single-cell type classifier trained on the automatically generated SegPath cell dataset, compared to NuCLS expert level annotations, with final evaluation on the NuCLS corrected single-rater test set for lymphocytes.

Dataset	Network	mF ₁ \pm SD	Lymphocyte			Other		
			F ₁ \pm SD	Prec \pm SD	Rec \pm SD	F ₁ \pm SD	Prec \pm SD	Rec \pm SD
NuCLS Base	SAM-H	0.769 \pm 0.012	0.693 \pm 0.020	0.595 \pm 0.047	0.839 \pm 0.052	0.846 \pm 0.006	0.793 \pm 0.021	0.908 \pm 0.029
	HIPT ₂₅₆	0.742 \pm 0.011	0.652 \pm 0.020	0.555 \pm 0.037	0.795 \pm 0.047	0.832 \pm 0.005	0.764 \pm 0.018	0.916 \pm 0.021
	UNI	0.756 \pm 0.004	0.673 \pm 0.006	0.590 \pm 0.018	0.787 \pm 0.035	0.839 \pm 0.003	0.767 \pm 0.011	0.928 \pm 0.011
SegPath	SAM-H	0.743	0.651	0.625	0.679	0.836	0.751	0.943
	HIPT ₂₅₆	0.713	0.603	0.490	0.783	0.824	0.770	0.887
	UNI	0.738	0.642	0.532	0.809	0.834	0.779	0.897

Table S14. Performance of the single-cell type classifier trained on the automatically generated SegPath cell dataset, compared to NuCLS expert level annotations, with final evaluation on the NuCLS corrected single-rater test set for plasma cells.

Dataset	Encoder	mF ₁ ± SD	Plasma Cell			Other		
			F ₁ ± SD	Prec ± SD	Rec ± SD	F ₁ ± SD	Prec ± SD	Rec ± SD
NuCLS Base	HIPT ₂₅₆	0.654 ± 0.075	0.486 ± 0.134	0.641 ± 0.112	0.432 ± 0.195	0.822 ± 0.017	0.715 ± 0.026	0.968 ± 0.013
	UNI	0.745 ± 0.042	0.651 ± 0.075	0.740 ± 0.073	0.594 ± 0.117	0.838 ± 0.009	0.738 ± 0.015	0.971 ± 0.005
	SAM-H	0.682 ± 0.033	0.524 ± 0.060	0.644 ± 0.041	0.449 ± 0.090	0.839 ± 0.006	0.742 ± 0.012	0.967 ± 0.005
SegPath	HIPT ₂₅₆	0.582	0.354	0.668	0.240	0.811	0.692	0.980
	UNI	0.723	0.606	0.612	0.600	0.841	0.747	0.961
	SAM-H	0.740	0.632	0.653	0.613	0.848	0.760	0.960

Table S15. Summary of cell annotations in the PanopTILs dataset split by cell type and data split.

	TILs	Stromal	Epithelial	Miscellaneous
Train	197,617	237,483	338,251	41,535
Test	14,237	7,986	16,704	5,946

Table S16. PanopTILs reference results of our CellViT⁺⁺ models, split across cell types.

		CellViT ⁺⁺ _{HIPT₂₅₆}	CellViT ⁺⁺ _{UNI}	CellViT ⁺⁺ _{SAM-H}
		TILs	F ₁ ± SD	0.792 ± 0.005
	Precision ± SD	0.843 ± 0.012	0.845 ± 0.008	0.846 ± 0.010
	Recall ± SD	0.747 ± 0.019	0.760 ± 0.017	0.760 ± 0.016
Epithelial	F ₁ ± SD	0.785 ± 0.009	0.787 ± 0.005	0.800 ± 0.003
	Precision ± SD	0.858 ± 0.011	0.827 ± 0.007	0.868 ± 0.008
	Recall ± SD	0.723 ± 0.021	0.750 ± 0.007	0.741 ± 0.010
Stromal	F ₁ ± SD	0.632 ± 0.003	0.634 ± 0.006	0.643 ± 0.006
	Precision ± SD	0.563 ± 0.009	0.549 ± 0.017	0.584 ± 0.017
	Recall ± SD	0.721 ± 0.012	0.751 ± 0.018	0.716 ± 0.017
Other	F ₁ ± SD	0.278 ± 0.023	0.247 ± 0.026	0.242 ± 0.023
	Precision ± SD	0.545 ± 0.033	0.603 ± 0.036	0.560 ± 0.024
	Recall ± SD	0.189 ± 0.024	0.157 ± 0.021	0.155 ± 0.020

Table S17. MIDOG⁺⁺ precision values.

Models		CellViT ⁺⁺ _{SAM-H}	CellViT ⁺⁺ _{SAM-H}	CellViT ⁺⁺ _{SAM-H}
Organs	Origin	No Additional Cells	20 Additional Cells	200 Additional Cells
Breast Cancer		0.73 (SD 0.03)	0.79 (SD 0.01)	0.77 (SD 0.04)
Neuroendocrine Tumor	Human	0.47 (SD 0.14)	0.53 (SD 0.03)	0.54 (SD 0.07)
Melanoma		0.74 (SD 0.21)	0.75 (SD 0.04)	0.83 (SD 0.03)
Cutaneous Mast Cell Tumor		0.65 (SD 0.14)	0.73 (SD 0.05)	0.73 (SD 0.04)
Lung Cancer	Canine	0.36 (SD 0.07)	0.41 (SD 0.04)	0.42 (SD 0.06)
Lymphoma		0.61 (SD 0.09)	0.60 (SD 0.05)	0.59 (SD 0.04)
Soft Tissue Sarcoma		0.71 (SD 0.03)	0.75 (SD 0.02)	0.71 (SD 0.03)

Table S18. MIDOG⁺⁺ recall values.

Models		CellViT ⁺⁺ _{SAM-H}	CellViT ⁺⁺ _{SAM-H}	CellViT ⁺⁺ _{SAM-H}
Organs	Origin	No Additional Cells	20 Additional Cells	200 Additional Cells
Breast Cancer		0.38 (SD 0.05)	0.42 (SD 0.02)	0.49 (SD 0.03)
Neuroendocrine Tumor	Human	0.33 (SD 0.08)	0.39 (SD 0.02)	0.48 (SD 0.06)
Melanoma		0.56 (SD 0.10)	0.60 (SD 0.03)	0.62 (SD 0.03)
Cutaneous Mast Cell Tumor		0.63 (SD 0.07)	0.61 (SD 0.03)	0.68 (SD 0.03)
Lung Cancer	Canine	0.34 (SD 0.06)	0.41 (SD 0.03)	0.44 (SD 0.02)
Lymphoma		0.39 (SD 0.05)	0.44 (SD 0.03)	0.57 (SD 0.05)
Soft Tissue Sarcoma		0.43 (SD 0.06)	0.42 (SD 0.01)	0.48 (SD 0.04)

Table S19. List of classical machine learning models evaluated using the PyCaret automated machine learning (AutoML) framework for the Lizard dataset. CatBoost classifier (marked bold) was the best performing model among all tested.

Model	
1	Logistic Regression
2	Linear Discriminant Analysis
3	Ridge Classifier
4	Ada Boost Classifier
5	Gradient Boosting Classifier
6	CatBoost Classifier
7	Extreme Gradient Boosting
8	Light Gradient Boosting Machine
9	Quadratic Discriminant Analysis
10	Random Forest Classifier
11	Decision Tree Classifier
12	Extra Trees Classifier
13	K Neighbors Classifier
14	Naive Bayes
15	SVM - Linear Kernel

Table S20. Overview of augmentation techniques used in the study. This table lists the augmentation techniques along with their corresponding Albumentations function names, the probability of application, and relevant parameters for each technique.

Augmentation Technique	Albumentations Function Name	Probability (p)	Parameters
Random Rotate 90	RandomRotate90	0.5	None
Horizontal Flip	HorizontalFlip	0.5	None
Vertical Flip	VerticalFlip	0.5	None
Downscale	Downscale	0.15	scale_max = 0.5, scale_min = 0.5
Blur	Blur	0.2	blur_limit = 10
Gaussian Noise	GaussNoise	0.25	var_limit = 50
Color Jitter	ColorJitter	0.2	brightness = 0.25, contrast = 0.25, saturation = 0.1, hue = 0.05
Superpixels	Superpixels	0.1	p_replace = 0.1, n_segments = 200, max_size = h/2
Zoom Blur	ZoomBlur	0.1	max_factor = 1.05
Random Sized Crop	RandomSizedCrop	0.1	min_max_height = (h/2, h), height = h, width = w

Table S21. Summary of the cell datasets used in this study.

Dataset	Cell Classes	Organs	Nuclei Amount	Patches/Slide Amount	Source	Resolution/Magnification	Seg-Mask	Note
Ocelot	Tumor, Non-tumor	Kidney, Head/Neck, Prostate, Stomach, Endometrium, Bladder	113,026	Total 303 Slides (173 train, 65 val, 65 test), cut into 663 tiles (400 train, 137 val, 126 test) with size 1024 × 1024	TCGA	0.25 μm/px / ×40	No	The authors removed 4 test tiles due to missing annotations
MIDOG++	Mitotic figures, Non-mitotic figures	Breast (Human), Neuroendocrine Tumor (Human), Melanoma (Human), Cutaneous Mast Cell Tumor (Canine), Neuroendocrine Tumor (Canine), Lymphoma (Canine), Soft Tissue Sarcoma (Canine)	26,289 annotated, 7,398,795 total	503 images with various sizes, average of 6,804 × 5,102 pixels	UMC Utrecht, VMU Vienna, FU Berlin, AMC New York	0.23 μm/px - 0.25 μm/px	No	-
CoNSEP	Epithelial, Inflammatory, Spindle-shaped, Miscellaneous	Colon	24,332	41 patches (27 train, 14 test) with size num1000 × num1000	University Hospitals Coventry and Warwickshire (UK)	0.25 μm/px / ×40	Yes	Resized to num1024 × num1024
Lizard	Neutrophils, Lymphocytes, Plasma, Eosinophils, Epithelial, Connective	Colon	418,935	270 tiles of various sizes, 1016 × 917 pixels on average at 0.50 μm/px	University Hospitals Coventry and Warwickshire (UK), TCGA, China (Four)	0.50 μm/px / ×20	Yes	Resized from 0.5 to 0.25 with Lanczos filter at input and back to 0.50 μm/px at the output
NuCLS	Lymphocytes and Plasma (superclass: sTILs), Macrophages and Stromal (superclass: stromal cells), Mitotic and Non-Mitotic Tumor (superclass: tumor cells), Miscellaneous	Breast	48,365	109 train and 15 test WSI with 1-3 annotated crops, average crop size of 362 × 362 pixels, average FOV size (annotated area) of 320 pixels	TCGA	0.20 μm/px / ×40	No	Cropped just FOV area and resize to 256 × 256 pixels to achieve 0.25 μm/px
PanopTILs	TILs, Stromal, Epithelial, Miscellaneous	Breast	859,759	1709 train and 1317 test tiles, with size 1024 × 1024, but test tiles just annotated in a narrow FOV	TCGA	0.25 μm/px / ×40	No	-
Segpath	IF stainings of: Epithelial, Smooth muscle/Myofibroblasts, Lymphocytes, Leukocytes, Blood/lymphatic vessel, Plasma cells, Myeloid cells, Red blood cells	Bladder, Brain, Breast, Colon, Head/Neck, Kidney, Liver, Lung, Oesophagus, Ovary, Pancreas, Prostate, Sarcoma, Skin, Stomach, Testis, Thymus, Uterus	-	220 breast tiles for lymphocytes, 2054 for plasma cells with size 984 × 984	University of Tokyo Hospital	0.22 μm/px / ×40	-	No nuclei have been annotated. The dataset consists of registered HE and IHC stainings to automatically derive region-wise annotations. We extract nuclei annotations by transferring binary CellViT++ results to the IHC mask.

Table S22. Resources used in this study with identifier

Resource	Source	Identifier	Reference
CellViT++			-
Albumentations 1.3.0	Pip	albumentations.ai	Buslaev et al. (2018)
CatBoost 1.2.5	Pip	github.com/catboost/catboost	Dorogush et al. (2018)
cuCIM 24.04.00	Rapidsai (conda channel)	github.com/rapidsai/cucim	-
CuPY 13.2.0	Conda-forge (conda channel)	cupy.dev	Okuta et al. (2017)
GeoJSON 3.0.0	Pip	python-geojson.readthedocs.io/en/latest	-
huggingface-hub 0.22.2	Pip	huggingface.co	-
Numba 0.59.0	Pip	numba.pydata.org	Lam et al. (2015)
NumPy 1.23.5	Pip	numpy.org	Harris et al. (2020)
OpenSlide 4.0.0	Conda-forge (conda channel)	openslide.org	Goode et al. (2013)
openslide-python 1.3.1	Pip	openslide.org/api/python	-
opencv-python-headless 4.5.4.58	Pip	opencv.org	Bradski (2000)
pandarallel 1.6.5	Pip	github.com/nalepae/pandarallel	-
pandas 1.4.3	Pip	pandas.pydata.org	The pandas development team (2024)
PathoPatch 1.0.4b0	Pip	github.com/TIO-IKIM/PathoPatcher	Hörst et al. (2024b)
Pillow 10.3.0	Conda-forge (conda channel)	pillow.readthedocs.io	-
PyCaret 3.3.2	Pip	pycaret.org	Ali (2020)
Python 3.10.14	Conda-forge (conda channel)	www.python.org	-
Ray 2.9.3	Pip	www.ray.io	Moritz et al. (2018)
scikit-base 0.7.8	Pip	scikit-learn.org	Pedregosa et al. (2011)
scikit-image 0.19.8	Pip	scikit-image.org	Van der Walt et al. (2014)
scikit-learn 1.3.0	Pip	scikit-learn.org	Pedregosa et al. (2011)
scipy 1.8.1	Pip	scipy.org	Virtanen et al. (2020)
timm 1.0.8	Pip	timm.fast.ai	Wightman (2019)
torch 2.2.1	Pip	pytorch.org	Paszke et al. (2019)
torchmetrics 0.11.4	Pip	lightning.ai/docs/torchmetrics	Defleisen et al. (2022)
torchvision 0.17.1	Pip	/pytorch.org	-
ujson 5.8.0	Pip	pypi.org/project/ujson	-
WandB 0.15.4	Pip	wandb.ai	-
Wsidicom 0.20.4	Pip	github.com/imi-bigpicture/wsidicom	-
Wsidicomizer 0.13.2	Pip	github.com/imi-bigpicture/wsidicomizer	-
XGBoost 2.1.1	Pip	xgboost.readthedocs.io	Chen & Guestrin (2016)
Comparison Methods			-
SoftCTM	GitHub	github.com/lely475/SoftCTM (commit 8918beafd7d5a36695d1bbdb5bb8d6139376a4dc)	Schoenpflug & Koelzer (2024)
HoVer-Net	GitHub	github.com/vqdang/hover_net (commit 67e2ce5e3f1a64a2ece77ad1c24233653a9e0901)	Graham et al. (2019b)
Cerberus	GitHub	github.com/TissueImageAnalytics/cerberus (commit 5bccebb071bebd5911250034c94f3568f23f50bb)	Graham et al. (2023)
TIAToolBox	GitHub	github.com/TissueImageAnalytics/tiatoolbox (commit c180566bbe7ec04a9b91924748acf2d03f6302d9)	Pocock et al. (2022)
PointNu-Net	GitHub	github.com/Kaiseem/PointNu-Net (commit 747f5019df5f611e81a823e5318a2fa0b60e2571)	Yao et al. (2023)
Nucleii	GitHub	github.com/huangzhii/nucleii.io (commit 78d52270eaeb05bc26f9b134231431a04a837b22)	Huang et al. (2024)
CGIS-CPP			-
Foundation Models			-
HIPT	GitHub	github.com/mahmoodlab/HIPT (commit 7336ee7)	Chen et al. (2022)
UNI	Hugging Face	huggingface.co/MahmoodLab/UNI (commit ba5018a94088b378720cd07995efe65a79c6b952)	Chen et al. (2024)
Virchow	Hugging Face	huggingface.co/paige-ai/Virchow (commit b80411ffe0f1d3070879e512ffb0152d7997377)	Vorontsov et al. (2024)
Virchow2	Hugging Face	huggingface.co/paige-ai/Virchow2 (commit a8536e8a8dd3cd0b200aa44be674ef95d2ad1598)	Zimmermann et al. (2024)
Segment Anything	GitHub	github.com/facebookresearch/segment-anything	-
Datasets			-
Ocelot	Zenodo	zenodo.org/records/8417503	Ryu et al. (2023)
Midog++	Figshare	doi.org/10.6084/m9.figshare.c.6615571.v1	Auberville et al. (2023)
CoNSeP	HoVer-Net	warwick.ac.uk/fac/cross_fac/tia/data/hovern	Graham et al. (2019b)
Lizard	-	warwick.ac.uk/fac/cross_fac/tia/data/lizard	Graham et al. (2021)
NuCLS	-	sites.google.com/view/nucls/home	Amgad et al. (2022)
PanopTILs	-	sites.google.com/view/panoptils	Liu et al. (2024)
SegPath	-	dakomura.github.io/SegPath/ zenodo.org/record/7412529 zenodo.org/record/7412500	Komura et al. (2023)